International Journal of Greenhouse Gas Control 148 (2025) 104520

Contents lists available at ScienceDirect

International Journal of Greenhouse Gas Control

journal homepage: www.elsevier.com/locate/ijggc

The importance of whole system considerations for sustainable, long-term CO_2 injection and storage: Interplay between infrastructure-related corrosion and reservoir rock chemistry effects on the evolution of the CO_2 storage capacity

Frederick Pessu [a,*], Alice Macente [b], Olujide Sanni [a], Sandra Piazolo [c]

[a] School of Mechanical Engineering, University of Leeds, Leeds, UK
[b] School of Civil Engineering, University of Leeds, Leeds, UK. Now at the Department of Earth Sciences, University of Florence, Florence, Italy
[c] School of Earth and Environment, University of Leeds, Leeds, UK

ARTICLE INFO

Keywords:
Carbon capture and storage
Corrosion
Injection
Storage, Porosity, Permeability

ABSTRACT

As global emissions fail to reduce rapidly, Carbon Capture and Storage (CCS) is attracting ever-growing attention. CCS involves capturing, treating, transporting and storing CO_2 to ensure its long-term removal from the atmosphere. To design a viable CCS system, the different interactions and impacts of injected CO_2 (either as subcritical or supercritical fluid) across the whole CCS system need to be considered. However, it is unclear how changes in fluid chemistry and the pre-existing reservoir rock chemistry influence the evolution of the two key storage properties, porosity and permeability.

This study investigates how upstream corrosion-induced fluid chemistry changes and realistic rock composition could affect the injectivity and storage capacity of reservoirs. The condition and material chosen for this project fall into the possible envelope of conditions of interest during CO_2 injection and storage. Corrosion occurring during CO_2 injection through saline aquifers was simulated at 40 bar, 60°C for two weeks, using X65 carbon and ^{13}Cr steel. The fluid resulting from the experimental fluid-metal interaction was then reacted at ~40 bar, 60°C for another two weeks with two fine-grained arkoses, with and without lithic clast, representative of siliciclastic reservoir rocks.

Results show that upstream corrosion caused a change in fluid chemistry and decreased fluid acidity. The corrosion-induced chemical changes had a marked effect on the evolution of porosity and permeability within the reservoir rocks. The storage capacity of reservoir rocks with diverse mineralogy is highly dynamic, and directly affected by rock chemical composition and, importantly, the chemical evolution of the incoming fluid.

1. Introduction

Carbon Capture and Storage (CCS) in sealed geological formations is a key approach in a large-scale strategy for mitigating the impact of our dependency on fossil fuels for energy and reducing anthropogenic CO_2 release to the atmosphere (Tang et al., 2021)·(Kumar et al., 2020). It is deemed one of the most cost-effective solutions to reduce the net CO_2 emissions from industrial facilities. Several CCS projects are underway, including utilising depleted oil and gas fields (Kumar et al., 2020; Néel et al., 2022; Jayasekara et al., 2020) or saline aquifers (Tang et al., 2021; Kumar et al., 2020). Although the critical sequestration conditions for liquid CO_2 are 31 °C and 70 bar(Fentaw et al., 2024), there is also some variability of sequestration and storage conditions for specific CCS projects and geological formations(Jing et al., 2024) (Peter et al., 2022; Worden, 2024).

The main challenges are to retain the long-term resilience of the CCS system and make it cost-effective. In terms of transport infrastructure and storage integrity, two main problems need to be considered; namely (i) the potential of chemical reactions between CO_2-rich fluid and infrastructure material, which could result in significant corrosion of the infrastructure and (ii) the long-term porosity evolution of the storage site. Corrosion induced by impurities from captured CO_2 streams tend to cause further downstream degradation of materials used in the transportation and injection infrastructures (Wang et al., 2011, A. Razak

* Corresponding author.
E-mail address: f.o.pessu@leeds.ac.uk (F. Pessu).

https://doi.org/10.1016/j.ijggc.2025.104520
Received 9 June 2025; Received in revised form 19 September 2025; Accepted 31 October 2025
Available online 10 November 2025

et al., 2023) (Sun et al., 2023) (Sun et al., 2016). The accumulated effect of this sequence of metal – CO_2 stream interaction could therefore markedly affect the integrity of the penultimate CCS injection and final storage infrastructures with time. In addition, the low cost of steel and/or the dominance of steel-based materials within existing oil and gas infrastructure repurposed for CCS increases the risk of corrosion-induced changes in the chemistry and impurity content of the injected CO_2 stream. Furthermore, to ensure long-term sustainability of CO_2 storage, the storage site must maintain sufficient porosity, permeability, rock strength, composition of fluids, and heterogeneity level of the storage medium to allow injection without causing unwanted fracturing and CO_2 release (Heidarabad and Shin, 2024; Worden, 2024; Wang et al., 2023). Both potential issues are closely linked, as the chemistry of the CO_2 fluid that enters the storage site has a marked effect on the reactions and hence porosity evolution of the storage site itself (Fig. 1). It is important to note, that the evolution of pH through the CCS transport and storage system is expected to have a significant effect on the sustainability of the whole CCS system, as pH influences the reactivity or chemical aggression of any fluid (Pessu et al., 2015b).

In contrast to abundant corrosion-only studies, which increasingly point to the need for extremely high-purity CO_2 for safe and resilient transport infrastructure (Sun et al., 2023; Sun et al., 2016; Morland et al., 2022) despite the considerable cost penalty (Sonke et al., 2022), there is a lack of studies that investigate the effect and importance of corrosion-induced changes in fluid chemistry and impurities on the long-term performance of subsurface storage in a porous rock mass. Most corrosion-only studies focus only on the steel–brine interface with emphasis on material degradation rate and how the interface evolves with the formation of corrosion products of various chemistries(Sun et al., 2023). Such studies do not consider the effect of corrosion on the evolution of CO_2 fluid chemistry upstream to the injection and storage phase. CO_2-rock interaction–only studies focus on the evolution of porosity and permeability due to the balance of CO_2-fluid driven dissolution of rocks and precipitation of mineral phases due to the chemical heterogeneity in rocks (Wang et al., 2023; Peter et al., 2022). While the effects of CO_2 injection in the evolution of porosity and permeability of a realistic storage rock that is highly heterogenous (Wang et al., 2023) has been shown and continues to be explored, to the best of the authors' knowledge, to date there has been no study focused on the downstream effect of the accumulation of chemical impurities and changes in the chemistry of the CO_2 fluid stream (due to corrosion in the upstream phase) on the evolution of rock porosity and permeability through time.

This study fills this gap. It is a first-of-its-kind as, in a two phase approach, we investigate the injection phase of the CCS systems taking the cumulative effect of upstream corrosion of metallic components on the injection and storage properties of reservoir rocks into account. We experimentally simulated the point where injected CO_2–streams from upstream capture and transportation process meets the storage rocks to generate a new understanding of the evolution of CO_2-fluid rock behaviour with influence from upstream corrosion-related activities. In most cases, the dehydration process for these source CO_2 gas streams is <100 %. This means that there are ppm or ppb levels of moisture and other impurities within the CO_2 stream (Wang et al., 2011, A. Razak et al., 2023) which are capable of driving corrosion of steel. This occurs upstream of the injection phase, during which the CO_2 gas streams meet another water phase present in saline aquifers. This latter stage occurs during CO_2 injection, and before the CO_2-stream meets the storage

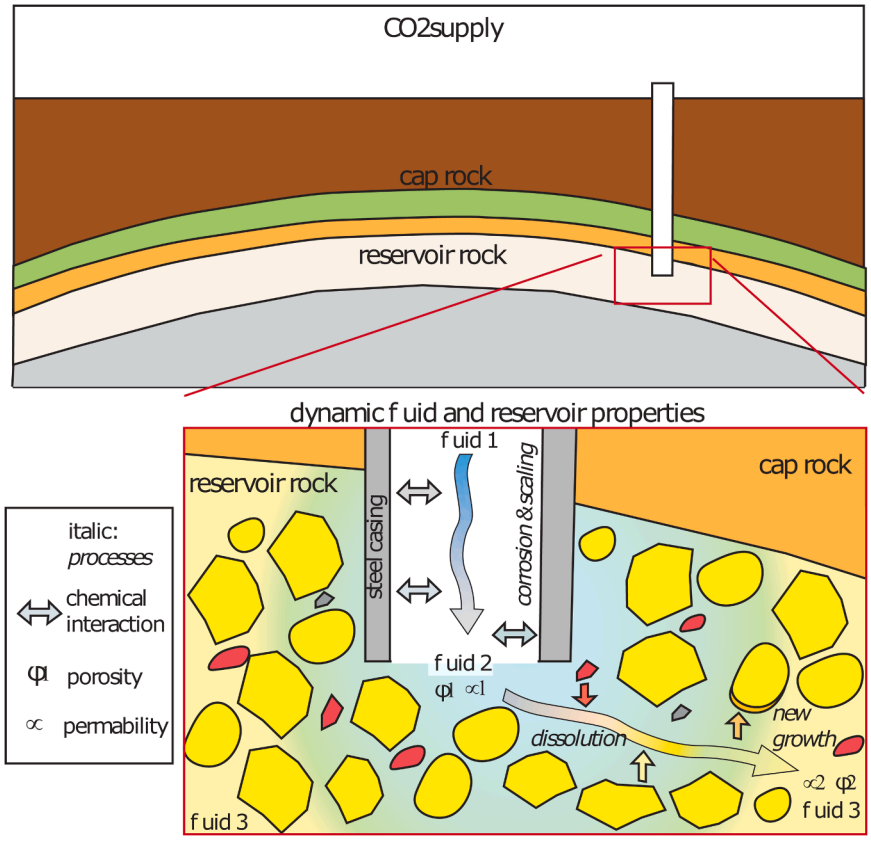

Fig. 1. Schematic diagram showing a CCS scheme, which includes CO_2 capture/supply at the Earth's surface, and transport within infrastructure dominated by pipes where pipe-CO_2 brine interaction occurs. Changes in the infrastructure occur, including scaling and corrosion, while the CO_2 brine changes composition in terms of trace elements and pH. The red box depicts a close-up of the CO2 brine-rock interaction at and near the entry point. Here, a series of different reactions occur due to the interaction of the CO_2 brine with the rock matrix, resulting in chemical and mineralogical changes within the rock matrix and changes in the CO_2 brine; note that any change in pH has a large impact on the reactivity of the brine.

rocks. Under the latter scenario, the CO_2 -stream that interacts with the rock is no longer dry but water-saturated/oversaturated. This scenario is the focus of this study.

We take a two-stage approach under static conditions. In *Stage I,* we react CO_2-rich fluid with two different infrastructure materials, namely carbon steel (X65) and 13 % Cr-alloyed steel (^{13}Cr). Here, we focus on the compositional change in the fluid due to the degradation of steel materials in interaction with the injected fluid. By using different steels, we capture the time-dependent changes in the chemistry of the CO_2 stream from capture to transportation caused by CO_2 fluid-metal interactions. In this case, we use X65 carbon steel to simulate the cumulative effect of long-term corrosion over a short experimental time. During *Stage II* we react representative natural rock samples from a former oilfield with the CO_2 fluid modified during Stage I. Although the experiments were performed under static conditions and were different from a more realistic flow-driven process, the findings from this study can provide an invaluable empirical understanding that can easily be translated to flow conditions.

Results from our work, a combined study of the interplay of fluid–metal interactions and corrosion-modified fluid-rock interactions within the CCS system, suggest that in-depth site-specific investigations are needed if we are to reliably predict the long-term resilience and sustainability of a CCS system.

In this study, our focus is on siliciclastic rocks, which are common in many countries, including the UK (Authority, 2025), where one of the main strategies for CCS is to use depleted oil fields for CO_2 storage. One of the financial advantages of repurposing depleted oil or gas fields is that much of the infrastructure can be repurposed as well, decreasing infrastructure costs markedly (Lam and Kuanji, 2023). A further potential benefit besides repurposing existing infrastructure is that, based on the accumulation of oil or gas in these areas, fluid is kept confined in known space, i.e. stored through geological traps such as impermeable cap rock, faults or geological structures such as fold hinges (Gussow, 1954). It is anticipated that, based on the proven geological stability of a former oil or gas field, storage of CO_2 will be safe in the future (Heidarabad and Shin, 2024). If CO_2 is not only stored in the pore space but also through the mineralisation of CO_2 trapping minerals, e.g. carbonates, then storage safety is increased (Hills et al., 2020). However, recent work by Worden (Worden, 2024) has shown that the well-studied behaviour of oil and gas within a storage site does not automatically mean that we know how the injected CO_2-saturated brine behaves in such depleted oil/gas fields. For example, it is still unclear how the porosity and permeability characteristics of the reservoir rock will change in time and space (Wang et al., 2023). This is also linked to the degree of variability in the impurities and conditions of CO_2 sequestration across different geological formations. For example, Rendel et al. (Rendel et al., 2018) presented a review of different conditions of CO_2-water-rock interactions relevant to CO_2 geological storage to highlight the potential variability in injection scenarios in different CCS projects. According to Michael et al. (Michael et al., 2010), the operating temperature for the Alberta Basin project in Canada is as low as 26 - 103 °C at injection depth of 950–2814 m and pressure of 60 - 270 bar. In this same report, the Ketzin project in Stuttgart, Germany operated at 34 °C at a depth of 650 m and injection pressure of 73 bar. In Salah Project, Krechba Formation in Algeria operated at 90 °C, at a depth of 1850 m and pressure of 179 bar. The test condition of 60 °C and 40 bar set in this project is inspired by the need to explore an average injection operation temperature from the various CCS projects around the world, particularly injection projects in Saline Aquifers, and a pressure range that allows us to perform this experiment with gaseous CO_2. Our study's aim is to establish a general methodology and generate findings that can be extrapolated to other more project specific conditions, particularly with supercritical CO_2 and other gaseous impurities. Furthermore, the naturally occurring reservoir rocks are usually not pure quartz sandstones, but heterogeneous, "impure" sandstones with significant proportions of other mineral phases such as feldspar, oxides, clays, some carbonates (calcite, siderite). Furthermore, remnant clasts of varying composition are common. Conceptually, in the case of impure reservoir rocks, the introduction of variable pure CO_2-saturated brine with variable chemistry and hence pH may trigger a series of different reactions at the storage site. pH may be decreased or increased depending on the specific reaction taking place, and porosity and permeability may subsequently increase or decrease.

2. Methods and materials

2.1. Analytical methods

2.1.1. Sample preparation: steel samples

Each of the steel samples used was sectioned into 15 mm x 10 mm x 5 mm blocks for ^{13}Cr and 15 mm x 10 mm x 3 mm blocks for X65 carbon steel (see below for details of steels used). All the samples were wet ground down to 1200 silicon carbide grit paper, degreased with acetone, rinsed with distilled water, and dried with compressed air before being assembled within the test set-up.

2.1.2. Sample preparation: rock samples

To assess the general mineral composition and microstructure of the chosen representative rock materials, we prepared polished thin sections of the representative samples as well as of the samples after exposing the rock to CO_2 brine. For *Stage II* tests, rock samples were cut into approximately 1 cm^3 cubes.

2.1.3. Brine - chemical analysis

Ex-situ pH of the brine was used in this study to track the changes in fluid chemistry due to corrosion of steel materials. Before every experiment, the Orion Star A111 pH meter/probe was calibrated. pH was measured at three stages of the whole experiment:

- Before *Stage I,* to represent fully CO_2-saturated brine,
- After *Stage I*, to assess the changes in fluid chemistry caused by CO_2-saturated brine-metal interactions, and
- After *Stage II,* to assess the changes in fluid chemistry caused by CO_2-saturated brine-rock interactions.

Atomic Absorption Spectroscopy (AAS) was used to measure the concentration of free Ca^{2+} remaining in the solution as an indication of $CaCO_3$ formation. For this project, 1 ml of the brine sample was taken before and after the experiment and added to 9 ml of a quenching solution to prevent further reaction of any unreacted Ca^{2+} ions. The quenching solution was prepared by dissolving 1 ml of Polyvinyl sulfonate (PVS) and 5.71 g of KCl in 1 L of distilled water. The pH of the quenchant was adjusted to be between 8 and 8.5 by adding drops of a 0.1 M NaOH solution, which was prepared by dissolving 0.4 g of NaOH in 100 ml of water. PVS and KCl both act to inactivate any potential reaction and provides ionic strength to stabilise the quenched samples, respectively. The potential reaction in this case is the oxidation of chemical species. Each component helps to retain the true state of the fluid without continuous degradation or modification of its chemistry

2.1.4. Sample analysis

General microstructure

Thin sections were assessed optically using a standard petrological microscope under plane and cross-polarisation light. Overview images were acquired by the OpticFilm8100 scanner.

SEM Imaging

For steel samples, the morphology and composition of the surface of the steel after the *stage I* test brine–metal interaction were investigated using a Carl Zeiss EVO MA15 scanning electron microscope. An incident beam voltage of 20 kV was employed at a working distance of 12–13 mm.

For rock samples, SEM imaging was conducted on thin sections of

pristine rock samples and on the same samples which were imaged through XCT, to confirm the spatial distribution of porosity and to identify any porosity change between fresh and carbonated samples. SEM analyses were conducted in a Zeiss Evo 15, with a working distance for imaging set at 8.5 mm and an energy of 20 kV.

Post-experiment Surface Analysis – steel samples

Composition of the newly grown phases on the steel sample was analysed using X-ray Diffraction (XRD), while the extent of pitting corrosion damage on the metal surface was also investigated using 3D – non-contact surface profilometry. A Bruker D8 X-ray diffractometer was used for XRD analysis of alloys to identify the corrosion product on the surface using monochromatic Cu Kα radiation (λ = 1.5418 Å). XRD patterns were collected in the 2θ range from 10° to 90° with a 1.5°/min scan rate.

X-ray Computed Tomography Imaging - rock samples

Rock samples were imaged before *Stage I* sequence, and after *Stage I – Stage II* experiments using X-ray Computed Tomography (XCT), to monitor and quantify the evolution of microstructure and storage properties, in particular volume and spatial distribution of porosity, pore connectivity and pore size distribution of the connected pores. XCT data were acquired in a Zeiss Versa Xradia 410 hosted in the School of Civil Engineering, University of Leeds. All samples were scanned with a 0.4X magnifying lens, an x-ray energy of 80 kV and a power of 12 W. 1601 projections were acquired over a 360° rotation, with a 4-second exposure time per projection. The final reconstructed voxel size varied between 10 and 13 μm. Specific details per scan are reported in the Supplementary Material. Data were reconstructed using the automated Zeiss Reconstructor, and the analyses were carried out using Thermo Fisher Scientific Avizo® software.

2.2. Materials

2.2.1. Stage I: transport infrastructure experiments

Transport Infrastructure: Steel

API 5 L X65 carbon steel and ^{13}Cr (UNS41000) steel were used in the corrosion experiments. Table 1a presents the nominal chemical composition of the samples used for the corrosion experiments. Although the Cr-alloyed steel is the most common material used for CO_2 injection tubular and is less prone to corrosion than X65 carbon steel over short time scales (e.g. days and weeks), X65 steel was used in this study as it is more reactive; reactions are accelerated relative to Cr-alloyed steel. Consequently, it was possible to achieve fluid chemical changes (e.g. tracked through pH changes) simulating realistic long-term corrosion and corrosion-induced changes over a shortened experimental time.

CO_2-Saturated *Brine*

The brine composition for *stage I* experiments was designed to be a low-scaling brine where only an Iron-Calcium carbonate scale is expected to form (see Table 1b). Before the start of the experiments, the brine was deaerated with CO_2 gas at atmospheric conditions for a minimum of 12 h (usually overnight).

2.2.2. Stage II: storage reservoir samples - siliciclastic rock samples

All rock material stems from the Brent oil field core, specifically a suspended gas well (Mobil Well No 48/129–7, core No 5, Box No 53oF63; Chiswick Formation; location 65° 32′ 48.385′'N/01° 21′ 38.290′' E). Two types of samples were obtained: "arkose" sandstone (sample A, 9861 m), which exhibits no mm to cm scale clasts; a sandstone with mm-cm scale clasts, termed in the following as "lithic arkose" (sample B, 9865 m). The section from which these samples are taken belongs to the Carboniferous, Westphalian. Cubes with maximum dimensions of ~8 mm were cut to be used in *Stage II- experiments*.

Rock sample I - General arkose characteristics:

The arkose sandstone is characterised by 30–35 % feldspar, 50 % quartz, 10 % clay minerals after feldspar, and 2–5 % oxides (Fig. 2a-c). It is an unsorted, very fine to fine sandstone. Grains are subangular to rounded, with grain boundaries often coated by very fine clay minerals. Porosity is visible (blue stain, Fig. 2a). Quartz and feldspar show slight undulous extinction in some grains (Fig. 2b). XCT scans of the starting material confirm the optical microscopy results (Fig. 2c). In the latter, the random distribution of oxides is seen as well as the low porosity.

Rock sample II - General lithic arkose characteristics:

The lithic arkose has up to 15 % lithic clasts, which are dominantly silt-sized siliciclastics. The arkosic matrix is similar to that of the arkose sample, with 30–40 % feldspar, 50 % quartz, 10 % clay minerals after feldspar, 2 % oxides (Fig. 2*d* – *f*). However, overall grain size is larger, the degree of sorting is poorer, and the porosity is higher and unevenly distributed (Fig. 2d). Grains and lithic clasts are subangular to rounded, with grain boundaries often decorated by very fine clay minerals. Quartz and feldspar show slight undulous extinction in some grains (Fig. 2e).

2.3. Details on experimental procedure and experiments conducted

2.3.1. Stage I: brine–steel interaction experiments

A total of six steel samples per litre of test solution were assembled in the vessel for the *stage I* experiments (refer to Fig. 3) in static conditions. The choice of static conditions ensured that any changes seen to materials and fluid chemistry are conservative with respect to an operating CCS system as flow-through conditions are expected to speed up the processes seen, as local chemical equilibrium is less likely to develop.

The CO_2-saturated brine was heated up to 60 °C before being transferred under a CO_2 gas atmosphere into the test vessel already containing the steel samples (Fig.3). The pH of the CO_2-saturated brine was measured at atmospheric pressure before being transferred into the Stage I vessel.

The assembled vessel holding the fluid and samples is then pressurised to 35 bars. There is always a temporary ~10 - 15 °C temperature loss during the fluid transfer process. This drop in temperature is completely recovered within 15 min after transfer by allowing the heating process to stabilise. The pressure then increases from 35 bar to 40 bar as the temperature increases from 45 °C to 60 °C. This phase of the experiment continues for two weeks (14 days).

After each static experiment, the steel samples were descaled to remove corrosion products using a standardised procedure that includes

Table 1
(a) Composition (wt. %) of transport infrastructure materials and (b) Initial brine composition.

(a) Elements	C	Mn	Si	Nb	Ni	P	S	Mo	V	Fe
API-5 L X65 carbon steel	0.15	1.422	0.22	0.054	0.09	0.025	0.002	0.17	0.057	Bal.
UNS41000 ^{13}Cr	0.15	0.56	0.36	-	-	0.006	-	-	-	Bal.

(b) Ion	Chemical formula	Mass (mg/L)
Na^{2+}	NaCl	31,275
Ca^{2+}	$CaCl_26H_2O$	2000
Mg^{2+}	$MgCl_2H_2O$	739
K^{+}	KCl	654

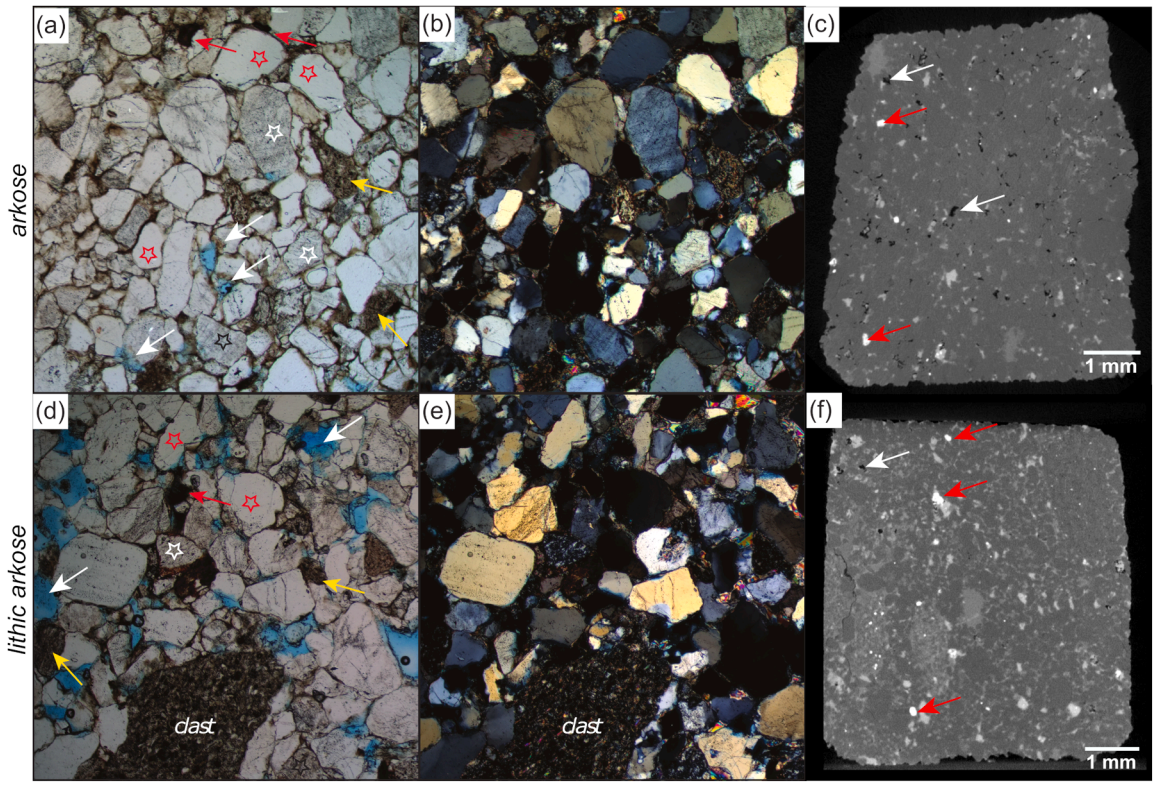

Fig. 2. Main microstructural characteristics of unreacted reservoir rock; Plane-polarised (a,d) and cross-polarised (b-e) optical images of arkose (a-b) and lithic arkose (d-e) samples: red and white stars depict quartz and feldspar grains, respectively; white, red and yellow arrows point to blue stained porosity, oxide grains and replaced feldspar by clay minerals, respectively; note high porosity and presence of mm scale clast. (c-f) Vertical XCT XZ slices of arkose and lithic arkose: again, white arrows indicate porosity (black voxels), red arrows indicate oxides: grey scale intensities identify quartz, feldspars and clay minerals, with the denser phases being the brightest.

using an ultrasonic bath with a solution of hydrochloric acid inhibited with 3.5 g/L of hexamethylene tetramine (HMTA) for two minutes.

Weight change and specific weight change based on weight before and after the immersion test were calculated via Eqs. (1) and (2)

$$\text{Weight Change } (\Delta w) = m_i - m_f \text{ (mg)} \quad (1)$$

Where m_i = initial weight and m_f = final weight after removal of corrosion products.

$$\text{Specific weight Change } Sw = (\Delta w)/A \text{ (mg/cm}^2\text{)} \quad (2)$$

Where A is the total exposed area of the steel samples.

We present data from two *Stage I* experiments, both conducted for two weeks at 60 °C and 40 bar: a) Stage I/X65: Interaction of initial CO_2-saturated brine with X65 steel samples, b) Stage I/^{13}Cr: Interaction of initial CO_2-saturated brine with ^{13}Cr steel samples.

2.3.2. *Stage II: modified CO_2-saturated brine–reservoir rock interaction experiments*

Cubes of each rock type were inserted together into an empty autoclave, separated by a ~5 cm distance and deaerated with CO_2 for up to 2 h.

After the completion of *Stage I* (i.e. CO_2-saturated –steel interaction tests for 2 weeks), the pressurised test vessel is slowly depressurised to atmospheric pressure and brine samples removed under a CO_2 atmosphere. Once the pH of the brine is measured post-Stage I, the brine is then transferred under a CO_2 atmosphere into the rock samples-containing autoclave, pressurised to an initial pressure of 35 bar, reheated to 60 °C and allowed to stabilise at 40 bar (Fig. 3). Stage II experiments were also performed in static conditions.

After the experiment is complete, the test vessel is slowly depressurised, and samples are removed, dried, and stored under vacuum before being processed for post-experiment analysis.

We present data from three *Stage II* experiments; all are conducted for two weeks at 60 °C and 40 bar: a*) Stage I – Stage II /X65 brine*: using the brine from the Stage I/X65 experiment (see above) and samples of both rock types, b) *Stage I – Stage II /*^{13}Cr brine: using the brine from the Stage I/^{13}Cr experiment, c) Stage II – only /brine$_{initial}$: using the initial CO_2-saturated brine and samples of both rock types.

3. Results

3.1. *Stage I: CO_2-saturated brine-steel interaction results in significant changes in CO_2 brine chemistry*

Figs. 4a and 4b present the results from corrosion of X65 carbon steel and ^{13}Cr alloyed steel in test conditions after two weeks of reaction with CO_2-saturated brine. Quantitative assessment of i) material degradation from brine-steel interaction was performed after removal of corrosion products, and ii) carbonate scales, using gravimetric analysis described by Eqs. (1) and 2. The result from this analysis is presented in the form of specific weight change (specific weight loss in this case) during the stage I experiment (Fig. 4a).

Specific weight loss was higher in carbon steel samples than in ^{13}Cr steel samples, which implies a higher rate of anodic dissolution of the ferrite phase. In Fig. 4b, the pH increases from ~3.5 to ~4.5 due to corrosion resulting from brine–steel interactions for ^{13}Cr and from ~3.5 to ~5.8 for carbon steel (X65). This represents a significant change in the chemistry of the brine due to the extent of corrosion of both steels and justifies the rationale for using carbon steel in this project. The change in pH data between pre-corrosion and post-corrosion for the two metallic samples correlates with the extent of loss of ferrous ions

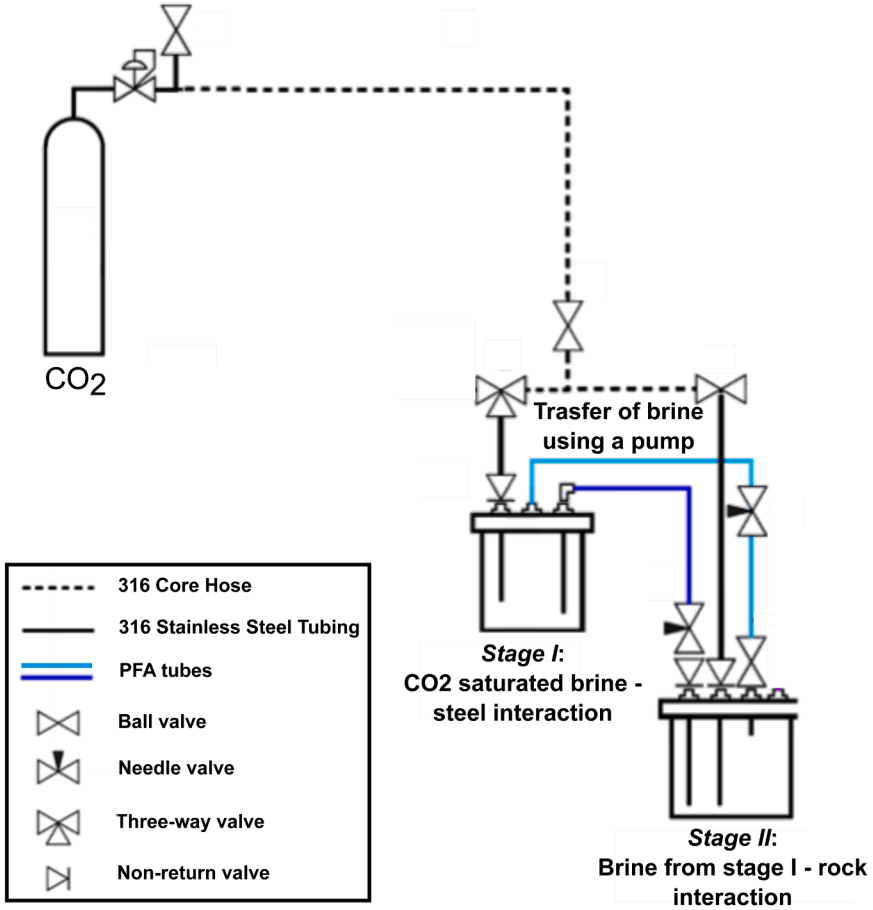

Fig. 3. Experimental set-up for simulating corrosion (brine–steel interaction Stage I) and carbonation (brine–rock interaction Stage II) experiments within the reservoir rock as fluid is injected.

indicated by the specific weight loss data in Fig. 4a.

In addition to the reported change in pH, the chemistry of the corrosion product on both metallic components is also different. Cr_2O_3 is expected to be a prominent corrosion layer in this condition for ^{13}Cr. However, a complex of Fe, Ca-CO_3 is formed on the surface of carbon steel, which is presented in Fig. 5a. This is also confirmed by the shift in key peaks for pure siderite ($FeCO_3$) at ~32 and 52.8 2θ to ~31 and 51 (Lavina et al., 2010). 2θ for $Fe_xCa_{1-x}CO_3$ is presented in Fig. 5b This represents a shift towards peaks for pure $CaCO^3$ at ~29 and 48.5 for pure $CaCO_3$ in which the degree of such shift is linked to the concentration of Ca^{2+} in the brine (Hua et al., 2018).

The process of formation of $Fe_xCa_{1-x}CO_3$ is also reflected in the AAS data presented in Fig. 4b showing a lower amount of free Ca^{2+} ions in the bulk fluid after the corrosion from brine–steel interaction for carbon steel than for ^{13}Cr. The new concentration of free Ca^{2+} ions and pH after corrosion becomes the inlet condition of the stage II experiments: brine – rock interaction.

Figs. 5e-f present 3D visual evidence showing the extent of corrosion damage in ^{13}Cr and X65 carbon steel samples, respectively. The rate of metal loss due to corrosion is significantly suppressed in ^{13}Cr, and its damage mechanism is restricted to pitting (Fig.5d), while the morphology of metal loss in X65 is more general (Fig.5e) with a substantial loss of material across the entire exposed surface.

3.2. Stage II: modified CO_2 brine-rock interaction changes rock properties

3.2.1. Evidence from XCT imaging: evolution of microstructures with CO2 injectivity

Bulk porosity evolution

In almost all experiments, porosity increases after Stage I: Brine-steel interaction /stage II: brine – rock interaction (Fig. 6a, 7). This increase is caused by an increase in internal close porosity (connected to the outside but connected below the voxel size), and by the appearance, in all cases, of newly formed open surface porosity after the experiments.

The arkose sandstone samples show an increase in total porosity of 0.3 vol. % and 2 vol. % after stage I and stage II experiment for the X65 carbon steel case, and for stage II - only experiment (without brine-steel interaction), respectively (Fig. 6a, 7a, 7b). The arkose sandstone presents 7 times increase of open surface porosity in the *stage II—only* experiment, while an appearance of 0.9 vol. % of open surface porosity and an increase of 4.5 times of overall total porosity in the *X65 stage I and stage II* experiment, post-experiment. It is evident from Figs. 7a, 7b that most of the increased porosity is localised at the edges of the samples in contact with the air and exposed to the brine. The evolution of porosity is particularly higher in the *stage II-only* experiment as seen in Fig. 7a.

In contrast, the lithic arkose sandstones behave quite differently. In the *stage II - only* experiment, this sandstone presents an increase in overall porosity by one order of magnitude before and after the experiment (from 0.1 vol % to ~1.3 vol %, Figs.. 6a, 7c); however, in the *X65 stage I and stage II* experiment, this dataset shows no significant difference in volume percentage of overall porosity content as compared to the remaining data, and no open pores are present at the end of the experiment (Fig. 6a, 7d). As evident from these figures, porosity inside the sample decreases with the experiment, while there is an increase of some minor porosity at the edges of the sample (Fig. 7c and 7d). Overall, the total volume of porosity remains unchanged (within errors) for this experiment and rock sample.

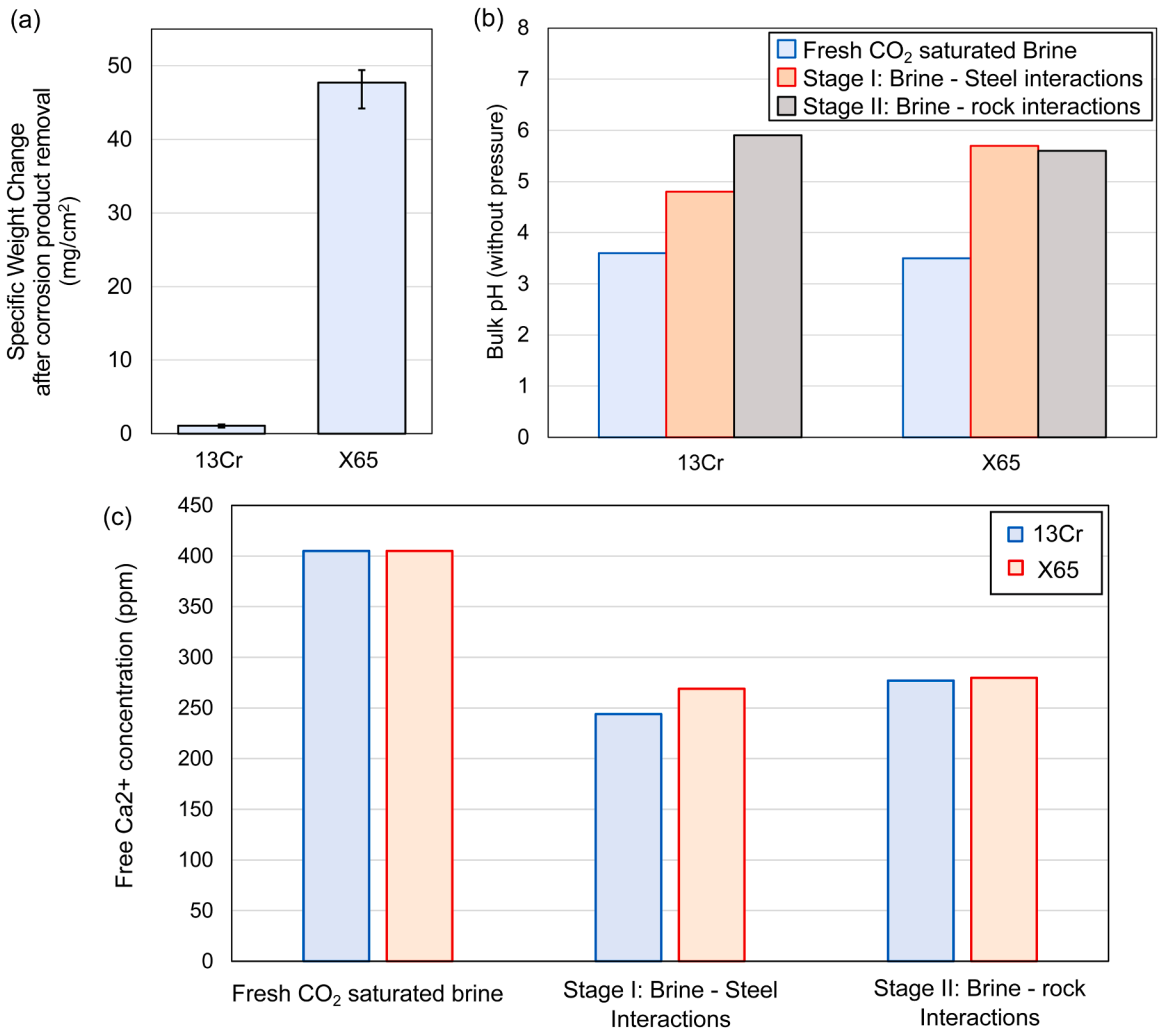

Fig. 4. (a) Specific weight changes after stage I: Brine–steel interaction experiments. (b) pH changes in fluid chemistry and (c) concentration of free Ca^{2+} ions (in data labels) due to stage I: Brine–steel interaction and stage II: Brine–rock interaction in Calcium carbonate forming CO_2 saturated brine at 60 °C and ~40 bar after 2 weeks.

In general, the results show evidence of the effect of brine – steel interaction in the form of corrosion on the evolution of fluid chemistry and the impact on the downstream reaction between brine and the rock samples. Total porosity increased 5-fold and 10-fold between brine – steel interaction experiments (X65: Stage I and Stage II) and brine – rock interaction experiments only (Stage II – only) for arkose sandstone and lithic arkose sandstone, respectively.

Pore Connectivity and Pore Size Evolution

In both experiments, the arkose sandstone samples show an increase in overall pore connectivity, in terms of the number of connected pores (labels) and the largest connected pore volumes (Fig. 6a, 8). For instance, in the *X65 Stage I – Stage II* experiment sequence, the number of labels increases from 2569 to 4483 post-experiment, with the largest connected pore volume increasing from 0.014 mm^3 to 0.03 mm^3, almost triple in size (Fig. 6b). This is evident from Fig. 8, where the same pores become connected and increase in size after the experiment. In the arkose *Stage II – only* experiment sequence, the number of connected labels increased by more than twice (Fig. 6d).

The lithic arkose sandstone sample shows, as the arkose sandstone, an increase in overall pore connectivity, number of connected pores and volume of the largest connected pore in *Stage II – only* experiment sequence, as evident from Fig. 6e. However, in the *X65 Stage I – Stage II* experiment sequence, the sample presents a decrease in the number and frequency of overall connected labels (from 5600 to 2300) (Fig. 6c). The size of the largest connected pore remains similar (from 0.0073 mm^3 to 0.0079 mm^3). It is therefore evident from the results of these experiments that lithic arkose sandstone sample presents a different outcome when compared to the arkose sandstone sample.

3.2.2. *Evidence from SEM imaging: evolution of microstructures with CO_2 injectivity*

After XCT scanning, the samples were cut in half, prepared as polished thin-section and then studied within the Scanning Electron Microscope. Back-scattered imaging shows that grain boundaries are notably larger and less tight in the rocks exposed to the CO_2 saturated brines (after stage II only test) (Fig. 9b - d, 10c-d) as compared to fresh samples (Fig. 9a, 9c, 10a). There is also a visible gradient of grain boundaries spacing which decreases away from the edges towards the centre of the sample (Fig. 9b, 9d, 10b). Grain boundaries are also visibly more rounded in the samples after stage II only test compared to fresh samples, as indicative of dissolution (Fig. 9e, 9f, 10d). These microstructural differences are present in both sequences of experiments, and in both samples (Fig. 9, 10).

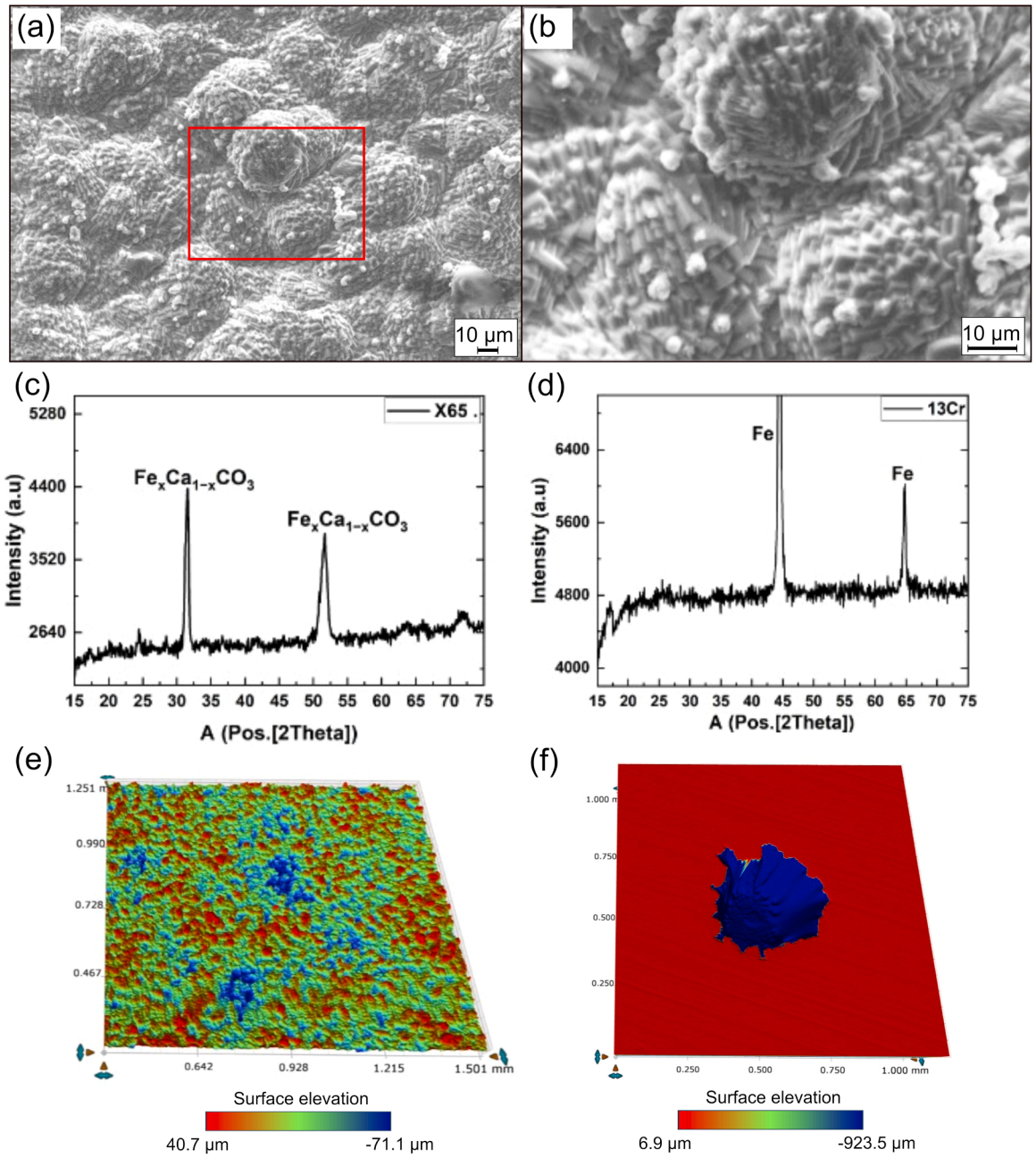

Fig. 5. Characteristics of changes in steel materials after stage I Brine–steel interaction experiments: (a) SEM image of Ca co-precipitated siderite scales on X65; b) zoomed image of the red area in (a). (c-d) XRD patterns product of brine–steel interaction on X65 and ^{13}Cr, respectively. (e-f) surface topography showing the extent of material loss from X65 and ^{13}Cr, respectively. Experiments were performed at 60 °C and 40 bar for 2 weeks.

4. Discussions

4.1. Changes in brine chemistry driven by the interplay of material dissolution, brine buffering and scale precipitation

4.1.1. Stage I: changes in CO_2-saturated brine chemistry are driven by the interplay of material dissolution, brine buffering and scale precipitation

Referring to Figs. 4 and 5, it is evident that the rate of corrosion due to CO_2-saturated brine–metal interactions (in the form of specific weight loss) is higher in X65 carbon steel than in ^{13}Cr. This observation directly correlates to the rate of dissolution of the α-ferrite (Fe) phase from the bulk material (Pessu et al., 2020). The 3D images of the corroded surface in Fig. 5e for ^{13}Cr and Fig. 5f for X65 show a ferrite dissolution process occurring almost uniformly across the entire exposed surface area for X65 carbon steel and from a localised pit for ^{13}Cr. Most of the exposed surface area on ^{13}Cr is protected by the passivation of the surface due to the effect of alloying elements, including ^{13}Cr in the steel alloy(Sun et al., 2024), which suppresses the loss of material (Hua et al., 2016). On the other hand, the microstructure of X65 carbon steel is dominated by the α-ferrite phase (Pessu et al., 2022; Paolinelli et al., 2008), which is the phase that preferentially corrodes when in contact with corrosive fluids (Pessu et al., 2015a; Pessu et al., 2020; Paolinelli et al., 2008).

Metal loss linked to CO_2-saturated brine–steel interaction, enhances redox activities at the metal-brine interface, which involves the reduction of H^+ ions from hydrated CO_2 (in the form of carbonic acid: H_2CO_3) according to the following reactions:

Hydrolysis of CO_2

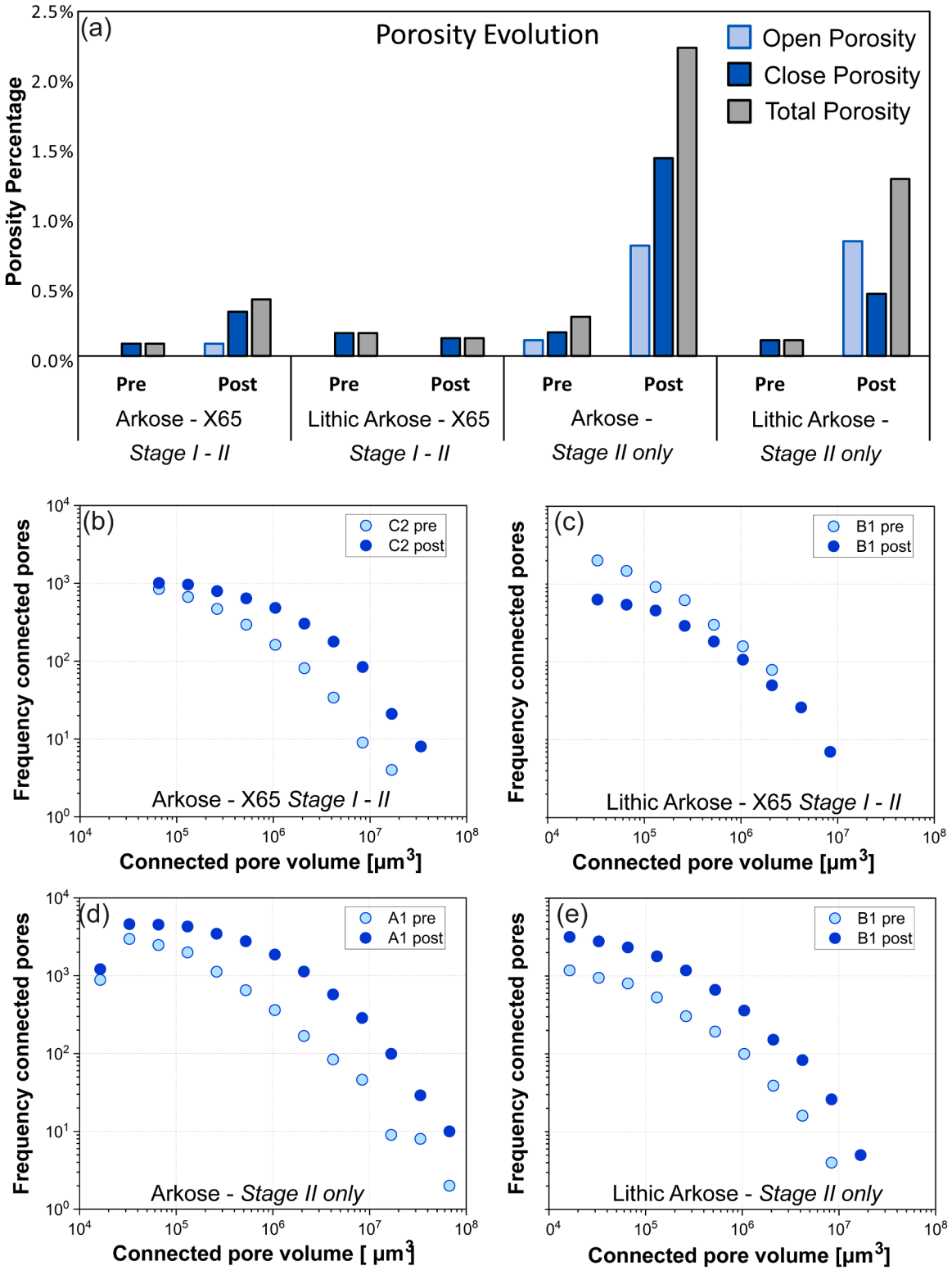

Fig. 6. (a) Summary of bulk porosity changes (in percentage) before and after stage II: Brine – rock interaction experiments for both arkose sandstone (C2) and lithic arkose sandstone (B1). Analysis performed for scenario with (for X65 only – Stage I / II) and without stage I; brine – steel interaction experiment (Stage II). (b – d) Frequency size distribution of connected pore volumes for arkose (b, d) and lithic arkose sandstone (c, e). Pore size distribution changes after stage I and stage II experiments for X65 (b - d), and only stage II experiment (d – e). Note that porosity increases in all cases after the experiment, except for the lithic arkose sandstone with X65 corrosion (c), which instead shows a decrease in porosity and pore size connectivity.

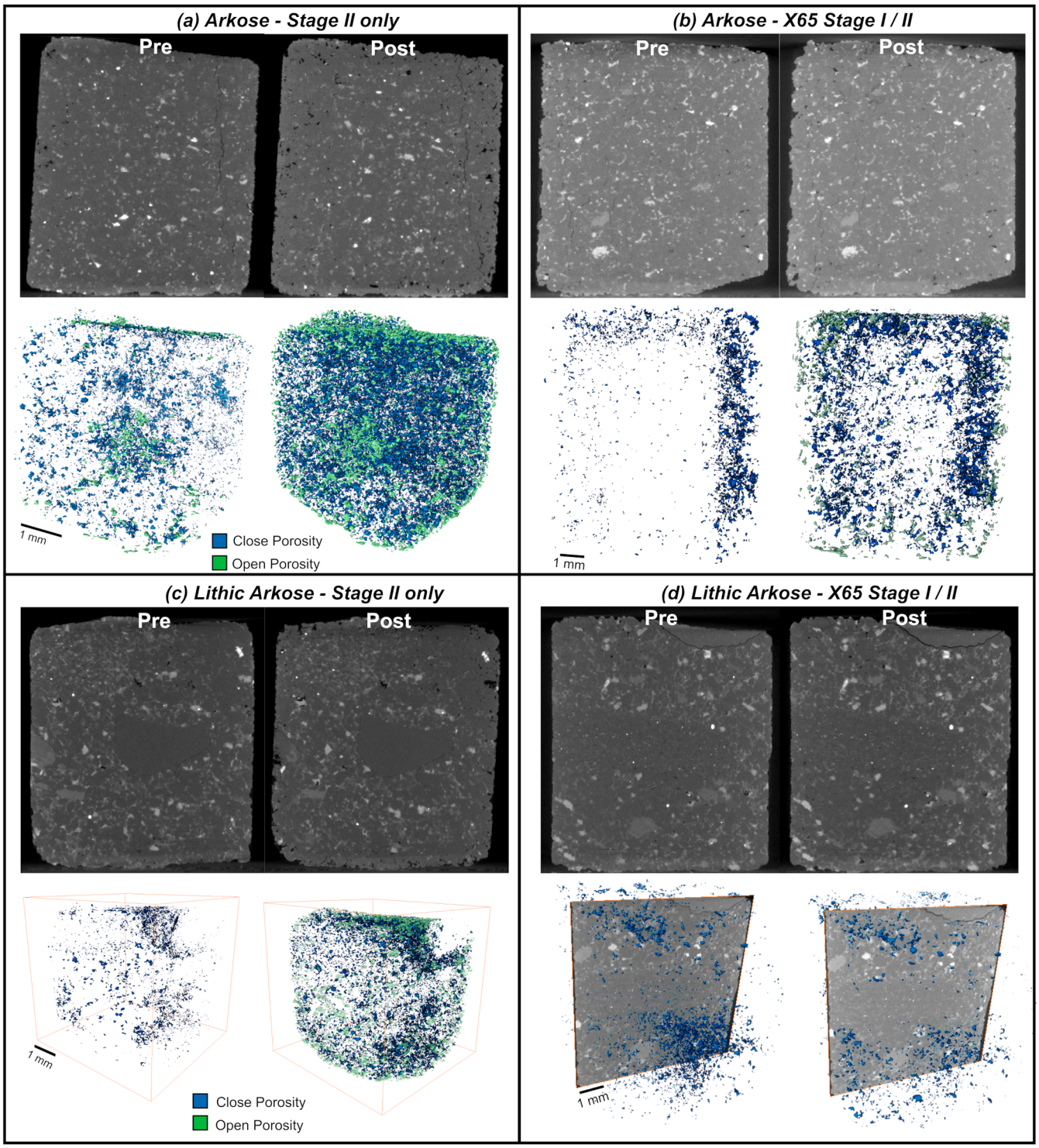

Fig. 7. Vertical XCT XZ slices and 3D renderings showing microstructural differences between the two samples and the two experiments, showing close porosity in blue and open-to-the-surface porosity in green. (a) Arkose sample, pre and post stage II – only experiment: Note the large porosity appearing along the edges of the sample post experiment; (b) Arkose sample, pre and post X65 stage I and stage II experiments: while it is less notable than in the Stage II – only experiment, appearance of porosity along the edges is visible post experiment; (c) Lithic arkose, pre and post stage II – only experiment; (d) Lithic arkose sample, pre and post X65 stage I and stage II experiments: note the absence of open porosity at the edges.

$$CO_2 + H_2O \leftrightarrow CO_2 - H_2O \equiv H_2CO_3 \leftrightarrow H^+ + HCO_3^- \quad (3)$$

(JAYASEKARA et al., 2020; KERMANI and MORSHED, 2003)

Anodic reaction:

$$Fe \rightarrow Fe^{2+} + 2e^- \quad (4)$$

Cathodic reaction:

$$H_2{:}CO_3 + 2e^- \leftrightarrow CO_3^{2-} + H_{2\,(g)} \uparrow \quad (5)$$

$$Fe + H_2CO_3 + 2e^- \leftrightarrow Fe^{2+} + CO_3^{2-} + 2e^- + H_{2\,(g)} \uparrow \quad (6)$$

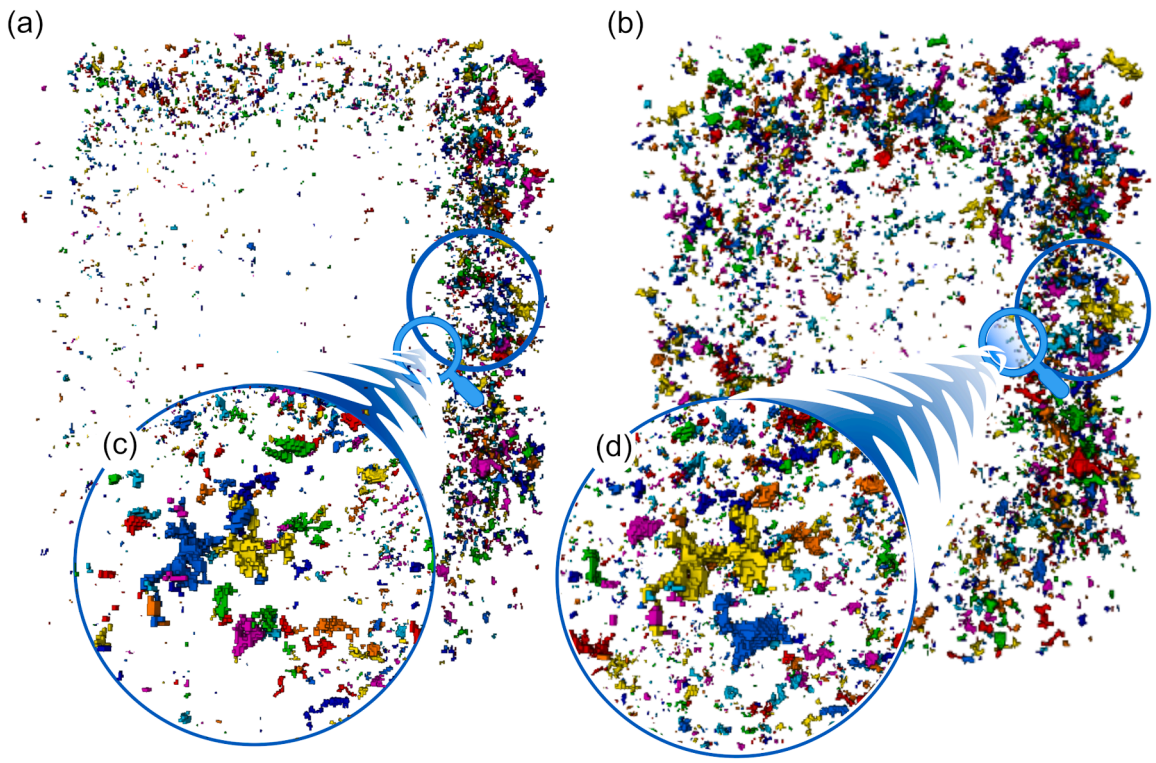

Fig. 8. Evolution of connected pore volumes before (a) and after (b) the X65 Stage I - II experiment in the arkose sandstone sample. Connected pore volumes are identified by the same colour: therefore, different colours indicate disconnected pore clusters. The same pores become larger and more connected after the experiment (onsets c, d).

$$Fe + H_2CO_3 \leftrightarrow FeCO_3 \downarrow + H_{2\,(g)} \uparrow \text{ ($FeCO_3$ film formation) (DE WAARD and MILLIAMS, 1975; KERMANI and MORSHED, 2003; NORDSVEEN et al., 2003)} \quad (7)$$

As shown by equations 4 – 7, the corrosion-induced mechanisms taking place during *stage I* brine–steel interactions remove H^+ as $H_{2(g)}$ out of solution and help to buffer the pH, changing the brine from acidic to alkaline. This is confirmed by the pH data shown in Fig. 4b Referring to Fig. 4, an increase in the metal loss process (measured as an increase in specific weight loss) increases the availability of ferrous ions (Fe^{2+}) in the bulk chemistry to drive the corresponding reduction of H^+ ions in solution as carbonic acid, and remove it as $H_{2(g)}$ according to Eqs. (5) and 6 (Pessu et al., 2015a) (Pessu et al., 2020). The difference in the rate of metal loss between ^{13}Cr and X65 carbon steel also correlates to the difference in the extent to which pH is increased because of their interaction with the CO_2-saturated brine. In Fig. 4bb, the pH increased from ~3.5 to ~4.8 after brine–^{13}Cr interaction but increased from ~3.5 to ~6 after brine–X65 interaction. This increase is higher in the X65 system due to the higher corrosion rate and hence higher redox activity than in the ^{13}Cr system. A schematic showing the mechanism of H^+ removal as $H_{2(g)}$ to cause an increase in pH is presented in Fig. 11.

As shown by Eq. (7), another consequence of these interfacial redox activities is the saturation of the bulk and near-surface of the carbon steel with Fe^{2+} and CO_3^{2-} ions for the formation of siderite scales ($FeCO_3$) as corrosion products in X65 carbon steel samples (Pessu et al., 2022; De Waard and Milliams, 1975)'(Kermani and Morshed, 2003). However, with the presence of Ca^{2+} in the brine (similar to most saline aquifers), there is also a competing impregnation of siderite by Ca^{2+} to alter the chemistry (see XRD peaks in Fig. 6e-f) and morphology of siderite from pure $FeCO_3$ to $Fe_xCa_{1-x}CO_3$ (see SEM image in Fig. 5a). A schematic of the Ca^+ impregnation of Siderite is presented in Fig. 11. The co-precipitation of $Fe_xCa_{1-x}CO_3$ therefore removes the Ca^{2+} from the fluid, as shown by the AAS data presented in Fig. 4b

Referring to Fig. 11, it is also plausible that $CaCO_3$ is nucleated in the bulk as well (Ogino et al., 1987). This process is described in Eq. (8).

$$Ca^{2+} + CO_2 - H_2O\ (H_2{:}CO_3) \leftrightarrow Ca^{2+}{:}CO_3^{2-} + H^+ \quad (8)$$

However, as this was not the focus of this study, the saturation ratio of the brine used was kept low as this was not designed to kinetically favour $CaCO_3$ crystal growth in the bulk. Therefore, the characterisation of $CaCO_3$ has not been prioritised in this study. The overall post-stage-I pH of the brine is therefore the result of the steel dissolution-induced increase in pH. This supports the observation of a larger increase in pH due to brine–X65 interaction than with the CO_2-saturated brine-^{13}Cr system shown in Fig. 4. With ^{13}Cr, the buffering effect leads to an order-of-magnitude less increase in H^+ ions compared to a 2-order-of-magnitude increase in H^+ ions with X65 carbon steel. This implies that the changes in chemistry of the brine post stage I test sequence is mainly driven by the buffering effect during the redox–induced dissolution steel components and by the extent of how much more ferrous ions is released during brine – steel interaction to drive the reduction of $2H^+$ to H_2 and increase the pH.

For X65, the consumption of free Ca^{2+} ions from the bulk is driven by a combination of the formation of $Fe_xCa_{1-x}CO_3$ from the redox and the chemical-driven processes in the bulk chemistry, as shown by the schematic representation of both mechanisms in Fig. 11. The impact of the confluence of these mechanisms presented in Fig. 11 is supported by the features observed in the cross-section of the outer edge of the X65 steel after *Stage I* test, as shown in Fig. 12. The edge, which represents the former interface between CO_2-saturated brine and steel, is characterised by two distinct layers. The inner layer has an irregular interface (grey dashed line, Fig. 12) with the intact steel and shows clear reduction in Fe but an increase in O and Ca relative to the steel; this layer is rich in siderite (iron-rich carbonate), however, some variation in siderite chemistry is seen. The outer layer is distinct in its homogeneous chemical nature and shows a razor-sharp boundary to the inner layers (white/black dashed line). We interpret the inner layer as the layer where Fe is

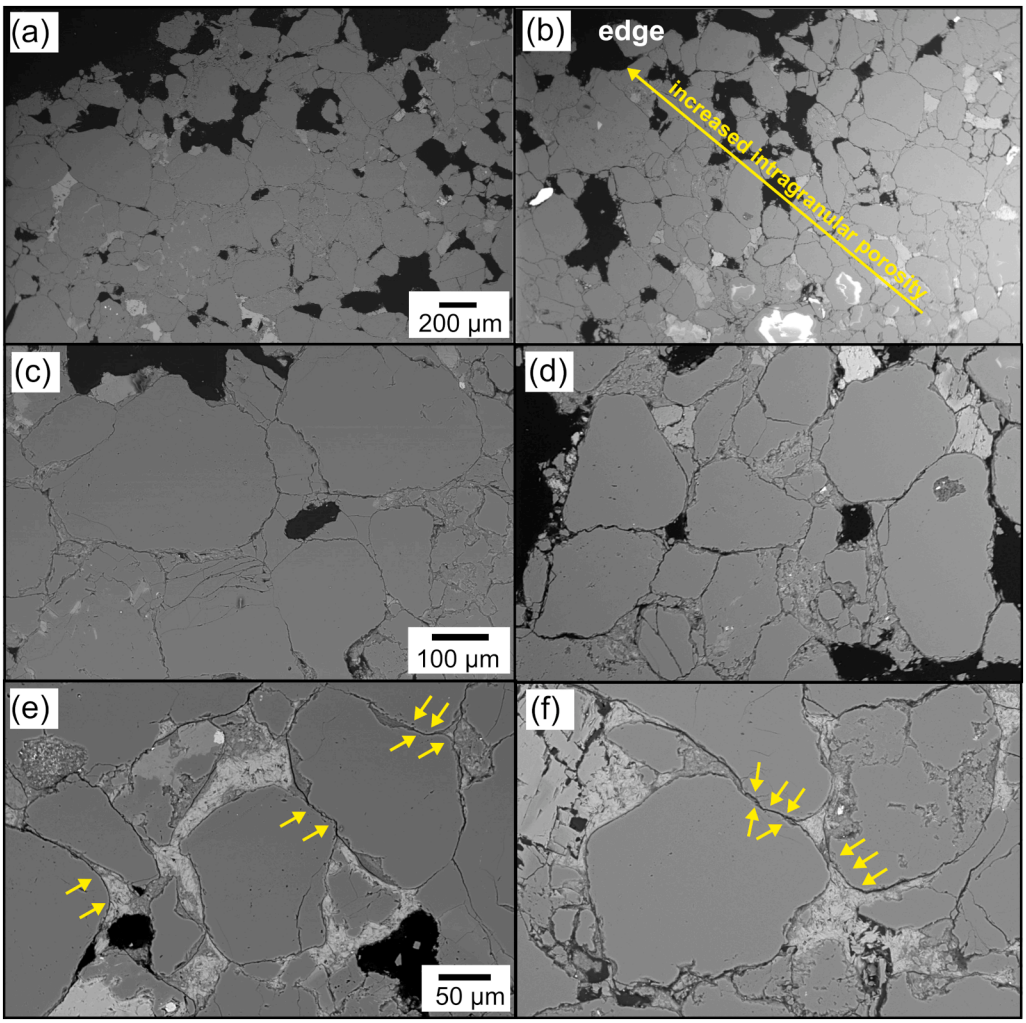

Fig. 9. Scanning Electron Back-Scattered Imaging of fresh arkose (a,c) and arkose samples after the Stage II – only experiment (b, d – f).

dissolved and Ca is co-precipitated to form siderite, while the second outer layer is caused by the rapid precipitation of siderite, forming a scale/overgrowth of siderite when the experiment is finished, and the fluid is depressurised (Fig. 12).

4.2. Stage II: downstream effect of changes in brine chemistry acquired during CO_2-saturated brine-transport infrastructure interaction on fluid–rock interaction within the reservoir environment

As the change of the CO_2-saturated brine after *Stage I* experiments is minor for ^{13}Cr steel, we restrict our discussion of *Stage II* fluid-rock interaction to the brine that reacted with X65 carbon steel during *Stage I*.

We would like to highlight that the purpose of this study was not to calculate the absolute change in porosity between *Stage I* and *Stage II* phases, and in the two rock compositions, but rather to demonstrate and highlight, through the use of the 3D imaging methods, how the overall microstructure, porosity and pore connectivity may evolve when we consider the combined effects of the upstream corrosion and downstream carbonation on the storage samples. The different minerals present in the samples play a critical role in the long-term evolution of these properties. Relatively small sample dimensions were required to allow a sufficiently good spatial resolution in the XCT imaging datasets. We chose dimensions that were a compromise between the representative volume of the samples and imaging resolution. The use of cm scale samples is consistent with the fact that large-scale processes often start at small-scale dynamics, where porosity, pore connectivity or permeability change dynamically in response to external physical or chemical processes (Macente et al., 2018) based on chemo-mechanical transformations (Macente et al., 2019), such as mineral replacement reactions, alteration of primary porosity, and/or creation of secondary porosity (Jamtveit and Austrheim, 2010; Jonas et al., 2014). Such transformations are at the core of reactive transport affecting rock microstructures (Yardley, 2009; Ghanbarzadeh et al., 2015; Gratier et al., 2013; Jamtveit and Austrheim, 2010; Kampman et al., 2014). In summary, while our choice of sample dimensions is consistent with the purpose of the study, the choice to conduct static experiments renders our results to be conservative relative to changes expected in response to a long-term CCS operation.

Referring to Fig. 4b, it is evident that the pH of the brine system without any corrosion of steel samples is highly acidic at a pH of ~3.6. This implies that only the chemical reaction that precedes $CaCO_3$ nucleation in the bulk and potential interaction with the chemical constituents within the rock samples (arkose - pure sandstone and lithic Arkose - impure sandstone) is likely to occur.

When compared to rock samples with pre-dissolution of X65 (i.e. *X65 Stage I - Stage II* experiments, Figs. 6, 7, 8), it is evident that the increase in pH due to the preceding metal dissolution process is lowering the rock dissolution kinetics as observed in the case of *Stage II* – only test sequence. For both Arkose and Lithic Arkose rock samples, the increase in porosity and pore connectivity is lower for *X65 Stage I - Stage II* experiments sequence than in the *Stage II – only* experiment sequence. The

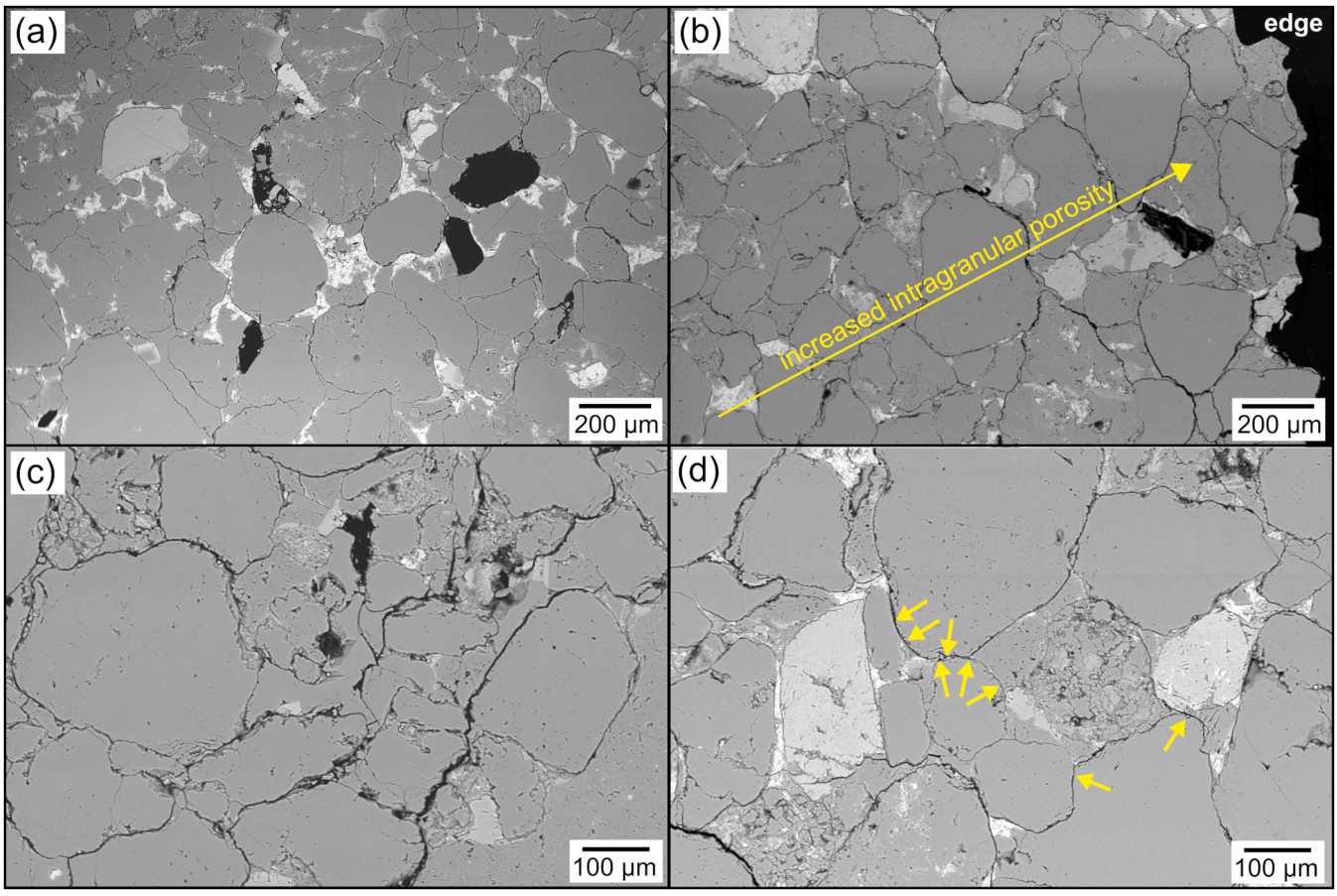

Fig. 10. Scanning Electron Back-Scattered Imaging of fresh lithic arkose (a) and lithic arkose samples after the X65 Stage I – II experiment (b – d). There is an increased gradient of porosity toward the edge of the sample after the experiment (b), grain boundaries are wider (c) and more rounded indicative of dissolution (d).

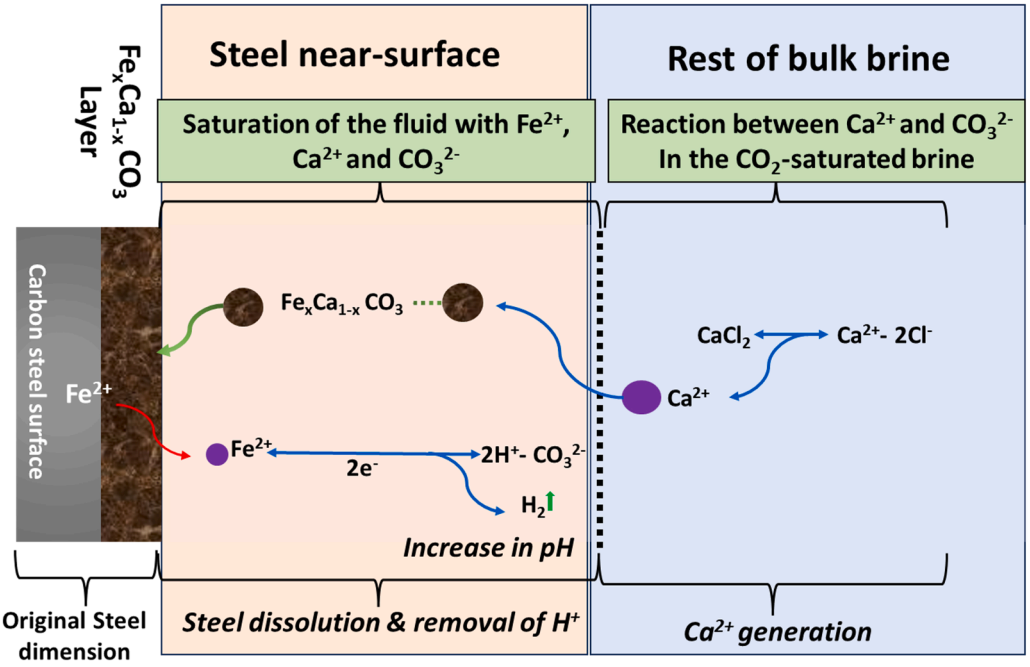

Fig. 11. Schematic illustration of the competition between the buffering effect of corrosion and the chemical-driven process of acidification during metal–CO_2 saturated fluid interactions. Note the different regions in the brine phase relative to the steel surface; in italic: processes.

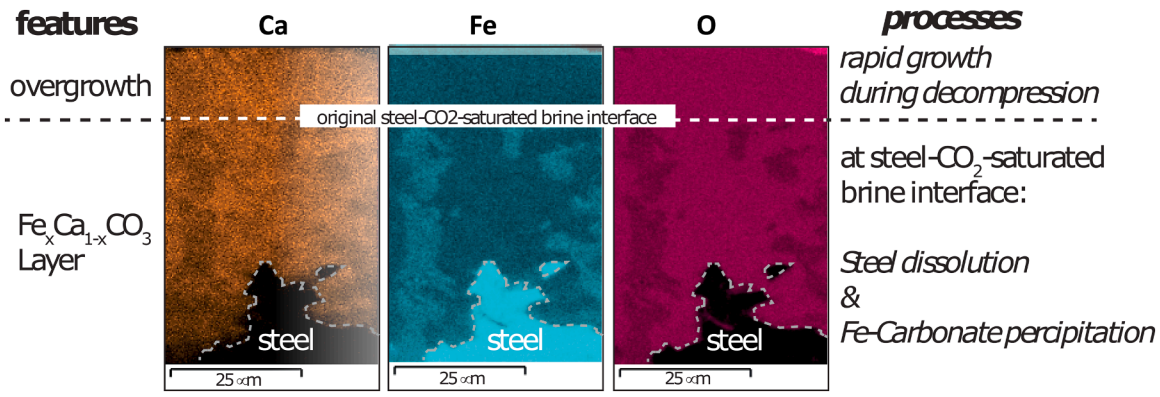

Fig. 12. Chemical composition of $Fe_xCa_{1-x}CO_3$ developed at the interface between carbon steel and CO_2 brine; Stage I corrosion experiment; in italic, processes are highlighted.

latter showed an increase of 5 and 10-fold in total porosity content for Arkose and Lithic Arkose rock as compared to Arkose and Lithic Arkose rock from *X65 Stage I – Stage II* experiment sequence. This lowered effect is caused by the increase in fluid pH due to the preceding metal dissolution process.

As shown in Fig. 4, the pH of the fluid before the CO_2-saturated brine reaction with rock samples increases from 3.6 with no preceding metal dissolution, to ~4.8 after the brine–metal interaction (with ^{13}Cr), and ~5.8 after the brine–metal interaction (with X65). This is shown to have the direct effect of decreasing porosity in the same order as shown in Fig. 13. An increase in pH in the brine with prior interaction with X65 carbon steel, leads to overall less carbonate dissolution and therefore less porosity increase in the rock. This observation correlates perfectly with an increase in metal dissolution rate from "no dissolution of metallic material" to a low dissolution rate of ^{13}Cr and a high dissolution rate of X65 carbon steel.

The pH evolution of the fluid before the CO_2-saturated brine reaction with rock samples impacts not only porosity but also pore connectivity. From the calculated pore connectivity results (Fig. 6, 8), it is evident that pore connectivity is increased in most cases except for the lithic arkose sample undergoing an X65 Stage I pre-corrosion history.

Although there is no *one-fit-to-all* porosity – permeability relationship in porous media and various geological processes may produce different porosity – permeability relationships (Bernabè et al., 2010), previous

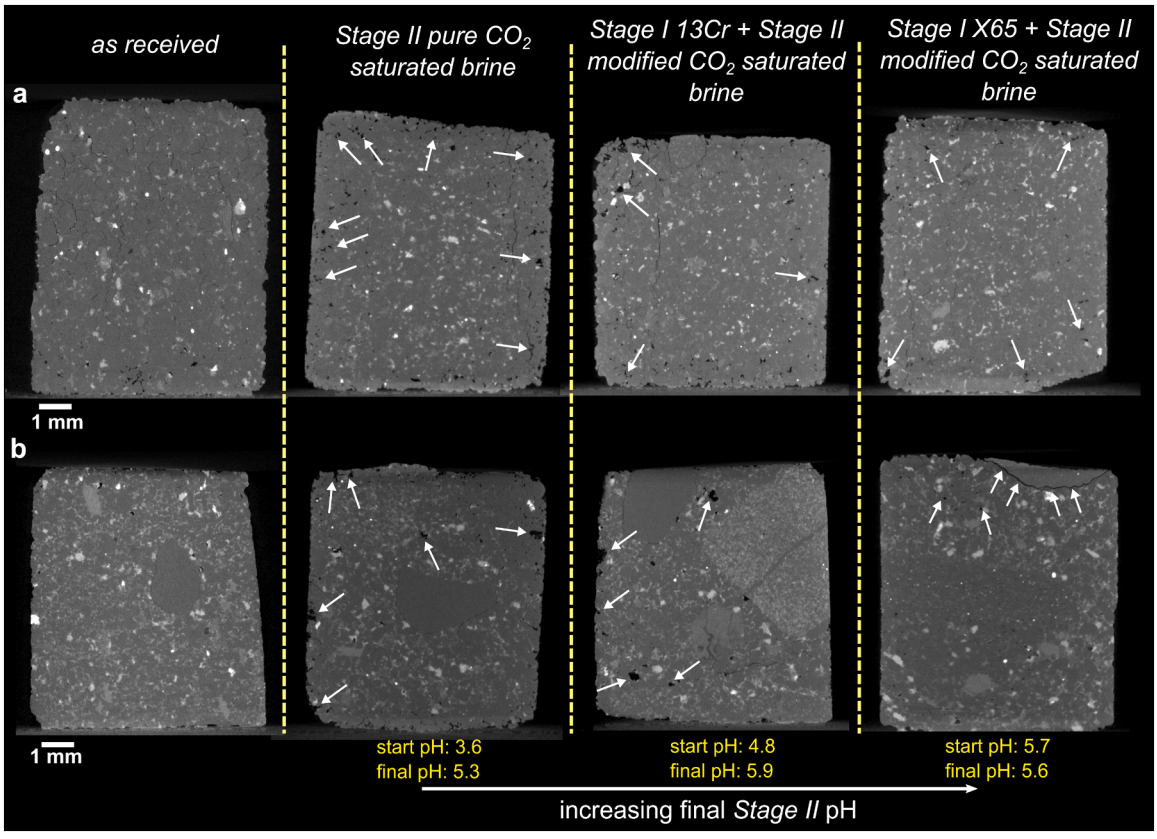

Fig. 13. Evolution of arkose sandstone (panel a) and lithic arkose sandstone (panel b) after Stage II (carbonation) with different types of Stage I history (no corrosion, 13 Cr corrosion and X65 corrosion). A fresh sample as a starting condition is also included. White arrows indicate new porosity. Note that the pH evolves with different types of Stage I history (starting values = Stage I, final values Stage II, all reported in yellow). pH value of the initial CO_2-saturated brine is 3.6 and does not change.

studies have shown that changes in the local pore microstructure (such as pore connectivity, pore throats etc.) are important factors in controlling permeability with a general positive correlation between pore connectivity and permeability (Bernabé et al., 2010, Clavaud et al., 2008). Thus, our data suggests that permeability is increased for those samples that show increased porosity i.e. all samples except for the lithic arkose sample undergoing an X65 Stage I pre-corrosion history. From Fig. 8, though, it is evident that the increase in pore connectivity is not sufficient to make the whole sample "permeable", as the sample porosity is not completely interconnected. The size of the sample and with that the resolution of our pore analysis may be limiting our ability to assess permeability as subvoxel pore connectivity may be present influencing whole system permeability. However, as Peng et al. (Peng et al., 2014) has shown, small pores do not influence permeability significantly but only contribute to changes in porosity and pore connectivity. Thus, we can assume our choice of resolution and sample dimensions is accurate for the purpose of studying the evolution of microstructure, porosity and pore connectivity during the coupled upstream corrosion-downstream carbonation.

The effect of corrosion-induced changes in brine pH and correlation to the evolution of rock porosity in this study is underpinned by the interaction of each mineral component of the rock with the CO_2-saturated brine. During CO_2-saturated brine interaction with rock minerals, particularly in the presence of carbonates and at pH $<$ 4, the geochemical dissolution of carbonates will occur according to Eqs. (9)–13 (Hassanzadeh et al., 2009), especially at temperature $\leq$60 °C (Jayasekara et al., 2020):

$$H^+ + H_2CO_3^- + CaCO_3 \leftrightarrow Ca^{2+} + 2H_2CO_3^- \quad (9)$$

$$H^+ + H_2CO_3^- + MgCO_3 \leftrightarrow Mg^{2+} + 2H_2CO_3^- \quad (10)$$

$$H^+ + H_2CO_3^- + FeCO_3 \leftrightarrow Mg^{2+} + 2H_2CO_3^- \quad (11)$$

$$H^+ + H_2CO_3^- + CaMg\,(CO_3)_2 \leftrightarrow Mg^{2+} + 2H_2CO_3 \quad (12)$$

$$SiO_2 + H_2O \leftrightarrow H_4SiO_4 \leftrightarrow H_2SiO_4^{2-} + 2H^+ \quad (13)$$

These reactions have the impact of increasing reservoir porosity and permeability, a key requirement for the viability of the long-term injection of CO_2 into saline aquifers. Carbonate dissolution at relatively low pH (~4) is the reason why there is an increase in porosity for rock samples during *stage II* (brine–rock interaction) only test sequence, as shown in Figs. 6 and 7.

Results from other CO_2 core-flooding experiments also observed carbonate dissolution at pH ~4.4, testified by the disappearance of calcite and ankerite mineral phases under SEM and XRD analyses (Yongzhi, 2012). Similar observations were noted by previous studies (Pearce et al., 1996; Assayag et al., 2009; Shiraki and Dunn, 2000). They also observed an abrupt increase of pH right at the beginning of the experiment, which could be linked to the long-term formation of new minerals (e.g. kaolinite), following dissolution of k-feldspars and albite and to the release of clay particles within the reacted brine after carbonate dissolution. These two phenomena together may be responsible for a reduction in permeability observed in the core-flooding experiments, while porosity remained unchanged. Similarly, in our experiments, the formation of new minerals such as kaolinite and clay minerals accumulated at pore throats (which could not be observed under XCT analyses due to resolution limits) may explain why porosity increase was lowered within the lithic arkose samples, testifying to a local dependency on the reservoir rock chemistry. Other studies (Peter et al., 2022; Ozotta et al., 2022), have shown that CO_2-brine interactions affect mineral composition, petrophysical, micromechanical and transport properties of reservoir rocks, and the effects differ with the chemistry of the reservoir rocks. Our results further strengthen the need for a complete assessment of CO_2-fluid-rock interactions, taking into consideration the various phases of changes in fluid chemistry along the whole CCS infrastructure.

4.3. Importance of pH evolution in CO_2-saturated brine-infrastructure and -reservoir rock interaction

The pH of injected fluid and the ensuing evolution within the whole CCS system, captured stream, transportation and injection, and storage, has been shown in this study to be of critical importance to the long-term viability of the CCS industry. As shown in this study, the pH of captured, transported and injected CO_2-rich fluids has a critical impact on the long-term integrity of the associated infrastructures in terms of upstream corrosion. This has also been shown in this study to have a direct influence on the long-term injection and storage capacity of CO_2 storage sites.

One of the key outcomes of this study is that the effect of pH across the whole CCS system is dynamic, in terms of its changes and impact during CO_2-saturated brine-infrastructure interaction and CO_2-saturated brine-reservoir rock interaction. During CO_2-saturated brine-infrastructure interaction, the pH of the CO_2-rich fluid changes with the extent of material corrosion. Therefore, effective material selection that suppresses upstream material corrosion can minimise the level of pH changes at this stage and maintain the relatively high acidity levels. However, this has been shown to have a corresponding impact on the long-term porosity and permeability of reservoir storage rocks.

Since this study was carried out under static conditions, in more realistic flow conditions, the rate of material loss due to corrosion is expected to increase due to increased mass transfer effect in increasing corrosion rate and preventing the formation of protective siderite layer. With an increase in flow velocity, the rate of accumulation of changes in fluid chemistry (in the form of bulk pH) may be initially slower, as most emerging chemical species are easily diluted by fresh streams of CO_2-rich fluids due to the mass transfer effect (Yan et al., 2024). However, this may later aggregate downstream within the rock pores with restricted flow paths during injection and storage to the same effect as observed in this study from static CO_2-fluid–rock interactions. While performing the tests under static conditions is one of the limitations of the approach in this study, the findings from this work closely represent a sped-up version of the same outcome expected under more realistic, long-term flow conditions.

It is clear, therefore, that if long-term porosity and increased injectivity are desired, the CO_2-saturated brine needs to remain low in pH throughout the CCS infrastructure-reservoir system. This highlights the need for in-line monitoring of the pH across the whole CCS system, and/or accurate modelling of the long-term evolution of the pH of transported and injected fluids. This will be critical for proactively determining the point of intervention to maintain porosity and rock injective capacity. However, if the operational target of the CO_2 storage site is to explore rock mineralisation to retain injected CO_2 in the trapped form, then a high pH fluid is desired. In both scenarios, it is imperative that the pH of the fluid, both within the infrastructure and the reservoir rock, is monitored and if need be, adjusted. This highlights the trade-off between the need for improved corrosion resistance, fluid chemistry and reactivity when interacting with reservoirs in CCS design. High corrosion resistance as shown in the case of stage I test with ^{13}Cr in this study, leads to lower buffering effect, maintaining fluid acidity and increasing the rate of dissolution of rock species. This has a direct correlation with increased porosity and permeability.

The overall rate of pH-driven geochemical reaction during CO_2-saturated brine-reservoir rock interaction is dependent on rock mineralogy, the chemistry (pH) of fluid, and the reservoir temperature and pressure. In addition, the presence of some impurities, such as NOx, SOx, and H_2S, can also accelerate the risks associated with storage and complicate the geochemical reactivity of the fluid (Ji and Zhu, 2013). For example, if hematite is part of the reservoir rock mineralogy, it will dissolve if in contact with H_2S, and consequently, porosity and permeability will increase (Kampman et al., 2016). Such a scenario would be desired for increasing injectivity but not for trapping injected CO_2 within a solid phase such as calcite.

4.4. Lessons learnt for CCS system planning and design

The findings from this research demonstrate a direct correlation between the dissolution of steel materials used for transporting and injecting CO_2 (upstream phase of CCS system) due to CO_2-fliuid-metal interaction, and the evolution of injection and storage properties of CO_2 storage reservoirs. Since this is an exploratory study, and ~99.95 % purity CO_2 gas stream has been used in this study, the results of changes in brine chemistry observed in this study can be an invaluable indicator of the potential impact of impurities such as NO_x O_2, SO_x and H_2S in more realistic CO_2 streams on the evolution of fluid chemistry and interaction with reservoir rocks, particularly CO_2 captured from a wide range of industrial processes(Néel et al., 2022).

Research on the impact of SOx by Hua et al. (2014) during the transportation phase of CCS systems, showed an increase in uniform metal dissolution rates (from 0.1 mm/yr to 0.7 mm/yr), and localised metal dissolution rates (from 0.9 mm/yr to 1.7 mm/yr) with an increase in SO_x and O_2 impurities up to 100 ppm and 20 ppm, respectively, in a water-saturated CO_2 stream. Similar to the modification of the morphology and chemistry of siderite formed in our study, $FeSO_3{\cdot}3\ H_2O$ was formed instead of pure siderite ($FeCO_3$). In a separate result published by the same author (Hua et al., 2016), It was established that for a wet CO_2 stream, there is a synergistic effect of multiple impurities (in this case, SO_2 and O_2) driving the increase in material degradation rate. This was consistent with the ISO-TR27921 (ISO-TR27921, 2020) Technical report, which summarises that the effect of SOx, NOx, O_2, CO and H_2S in transported and injected CO_2 streams is likely to increase the risk of localised material dissolution.

As shown in this study, an increase in metal dissolution rate correlates to an increase in the availability of ferrous ions to create a redox-induced buffering effect and change in injected fluid chemistry, particularly in terms of pH (Fig.4). Changes in fluid chemistry have been shown to induce changes in reservoir rock mineralogy, porosity and permeability (Tutolo et al., 2015). This is also found to depend on the specific initial mineralogy of the rock. For instance, where there is an increase in metal dissolution rate from this study, there is a significant increase in the fluid's pH and hence a lower rate of change in porosity due to the formation of new minerals, potentially kaolinite, and clay minerals which accumulated at pore throats within the lithic arkose rock samples due to its heterogeneity. Similar results of reprecipitation of minerals to cause pore throat blockage of sandstone during CO_2 flooding have also been reported (Wang et al., 2023). Therefore, any combination of impurities within the injected fluid that tends to increase metal dissolution rate, localised or uniform, from the capture, transportation and injection phase, is likely to induce similar changes to fluid chemistry as observed in this study. Furthermore, under fluid flow conditions, it is expected that the effect of impurities within the CO_2 stream will increase the metal degradation rate further (Yan et al., 2024). However, any potential changes in the fluid chemistry due to flow-enhanced corrosion may be initially suppressed by the mass transfer effects that take away any chemical species due to the corrosion process from the metal interface and aggregates downstream during injection (Yan et al., 2024). The aggregation of the effect of changes in fluid chemistry under flow conditions could transition to a static mode of CO_2 fluid-rock interaction, and mirror similar findings to those from this study.

The changes in reservoir rock storage properties observed in this study are therefore directly driven by a combination of changes in fluid chemistries due to brine–steel interactions and dynamic chemistries across different rock samples. This indicates the potential long-term impact of impurities such as CO_2 streams on the injectivity and storage capacity of CO_2 reservoirs, especially as NO_x, SO_x, O_2 and H_2S are expected to increase with the increase metal dissolution process during brine–steel interactions. This finding is corroborated by published CO_2 transport specification study, which concludes that it is nearly impossible to determine a "universal" CO_2 saturated brine specification and, by extension "ideal" rock characteristics to ensure long-term CO_2 storage (Morland et al., 2022). Dynamic changes in fluid chemistries must be considered throughout the whole CCS system; consequently, the approach taken in this study must be deployed and expanded to allow for the assessment of both operational and environmental constraints when assessing the long-term viability of CCS projects worldwide.

The authors are therefore proposing further research focused on investigating widely the different impurity levels and chemistry, and their effects on a wide range of subsurface reservoir rocks. This should also include investigating a wide range of CO_2 transport and injection conditions and a system for *in-situ* monitoring of changes in fluid chemistry linked to brine–steel interactions and brine–rock interaction in a single sequence. The authors are also proposing research programs focused on exploring in situ monitoring of pH (linked to changes in fluid chemistry) of fluid upstream to the reservoir rocks, and modelling of injection and storage properties of the reservoir. Such programs should be bespoke and matched against the specific objectives and operational circumstances of each CCS project. For instance, exploring in situ pH monitoring upstream to injection can be focused on reducing pH to improve injectivity; porosity and permeability in the initial stages of the CCS project, or focused on increasing pH to promote better trapping of CO_2 via mineralisation towards the end of the CCS project. Lastly, XCT imaging represents a highly valuable tool to investigate the 3D dynamic evolution of microstructures (porosity in this case), which would otherwise remain hidden and unobserved in other analytical techniques, hence providing highlights on where and how porosity may or may not increase in the sample, and how it evolved with the process. The measured values of initial porosity (and/or evolution of porosity/pore-connectivity) may be used as input in modelling, which often makes assumptions or simplifications on some known properties; results then may be compared with our direct imaging results, thus providing a direct tool of comparison.

5. Conclusions

Carbon Capture and storage (CCS) is deemed one of the most cost-effective solutions to reduce the net CO_2 emissions from industrial facilities. Successful CCS systems need to consider the different effects CO_2 has on the whole infrastructure (transport, injection and storage), as well as the microstructural changes within the subsurface reservoir rocks. In this study, we investigated the coupled mechanisms of interaction between transported/injected CO_2-rich upstream metallic infrastructure and the evolution of the injection and storage capacity of reservoir rocks. Our experiments evaluate how much impure systems, in this case upstream metal dissolution-induced fluid chemistry changes and rock chemistries, affect the storage capacity of reservoirs. Results show that:

- Upstream dissolution of metallic components caused a change in fluid chemistry and decreased fluid acidity after two weeks.
- This variation in CO_2 saturated brine chemistry has a direct impact on the evolution of porosity and pore connectivity within the storage matrix.
- The evolution of pH of transported and injected fluid is critical for ensuring the long-term injection and storage capacities of reservoir systems.
- Reservoir rock compositions may play an important role in driving further the evolution of storage capacity of reservoir rocks, prompting further studies focusing on the dynamic chemistries of reservoir rock.

Our findings focus attention on the need for integrative studies across the whole CCS system, also considering the presence of impurities (such as NO_x, SO_x and O_2) and the effects on reservoir rock chemistry.

CRediT authorship contribution statement

Frederick Pessu: Writing – review & editing, Writing – original draft, Supervision, Resources, Project administration, Methodology, Investigation, Funding acquisition, Formal analysis, Data curation, Conceptualization. **Alice Macente:** Writing – review & editing, Writing – original draft, Methodology, Investigation, Formal analysis, Data curation. **Olujide Sanni:** Formal analysis, Data curation. **Sandra Piazolo:** Writing – review & editing, Writing – original draft, Supervision, Resources, Project administration, Methodology, Investigation, Funding acquisition, Formal analysis, Data curation, Conceptualization.

Declaration of competing interest

No conflict of interest exists in the submission of this manuscript, and the manuscript is approved by all authors for publication. I would like to declare on behalf of my co-authors that the work described was original research that has not been published previously, and not under consideration for publication elsewhere, in whole or in part.

Acknowledgements

This project is funded by the Higher Education Innovation Funding through a work stream focused on STEM-driven solutions to climate change at the University of Leeds. XCT/SEM analyses were undertaken in the Centre for Infrastructure Materials, School of Civil Engineering, University of Leeds, UK, a UKCRIC Research Facility (EP/P017169/1). XRD Analyses were conducted in the Bragg Centre for Materials Research, University of Leeds, UK.

Data availability

Data will be made available on request.

References

ASSAYAG, N., MATTER, J., ADER, M., GOLDBERG, D., AGRINIER, P., 2009. Water–rock interactions during a CO2 injection field-test: implications on host rock dissolution and alteration effects. Chem. Geol. 265, 227–235.

AUTHORITY, N.S.T., 2025. Carbon Capture and Storage (CCS) is Critical to the UK Achieving Net Zero [Online]. Available. https://www.nstauthority.co.uk/the-move-to-net-zero/ccs. /[Accessed 12th May 2025 2025].

DE WAARD, C., MILLIAMS, D.E., 1975. Carbonic acid corrosion of steel. Corrosion 31, 177–181.

FENTAW, J.W., EMADI, H., HUSSAIN, A., FERNANDEZ, D.M., THIYAGARAJAN, S.R., 2024. Geochemistry in geological CO2 sequestration: a comprehensive review. Energies 17, 5000.

GHANBARZADEH, S., HESSE, M.A., PRODANOVIĆ, M., GARDNER, J.E, 2015. Deformation-assisted fluid percolation in rock salt. Science 350, 1069–1072.

GRATIER, J.-P., DYSTHE, D.K., RENARD, F., 2013. Chapter 2 - the role of pressure solution creep in the ductility of the earth's upper crust. In: DMOWSKA, R. (Ed.), Advances in Geophysics. Elsevier.

GUSSOW, W.C., 1954. Differential entrapment of oil and gas: a fundamental principle. AAPG Bull. 38, 816–853.

HASSANZADEH, H., POOLADI-DARVISH, M., KEITH, D.W., 2009. Accelerating CO2 dissolution in Saline aquifers for geological storage — mechanistic and sensitivity studies. Energy Fuels 23, 3328–3336.

HEIDARABAD, R.G., SHIN, K., 2024. Carbon capture and storage in depleted oil and gas reservoirs: the viewpoint of wellbore injectivity. Energies 17, 1201.

HILLS, C.D., TRIPATHI, N., CAREY, P.J., 2020. Mineralization technology for carbon capture, utilization, and storage. Front. Energy Res. 8. - 2020.

HUA, Y., BARKER, R., NEVILLE, A., 2014. Understanding the influence of SO2 and O2 on the corrosion of carbon steel in water-saturated supercritical CO2. Corrosion 71, 667–683.

HUA, Y., BARKER, R., BERMPERIDIS, G., ZHAO, H., NEVILLE, A., ZHANG, L., 2016. Comparison of corrosion behavior of X65, 1Cr, 5Cr and 13Cr steels in water-containing supercritical CO2 environments with SO2/O2. CORROSION 2016. NACE-2016-7681.

HUA, Y., SHAMSA, A., BARKER, R., NEVILLE, A., 2018. Protectiveness, morphology and composition of corrosion products formed on carbon steel in the presence of Cl−, Ca2+ and Mg2+ in high pressure CO2 environments. Appl. Surf. Sci. 455, 667–682.

ISO-TR27921 2020. Carbon dioxide capture, transportation, and geological storage — cross cutting issues — CO2 stream composition. Int. Organ. Stand.

JAMTVEIT, B., AUSTRHEIM, H.K., 2010. Metamorphism: the role of fluids. Elements 6, 153–158.

JAYASEKARA, D.W., RANJITH, P.G., WANNIARACHCHI, W.A.M., RATHNAWEERA, T. D., 2020. Understanding the chemico-mineralogical changes of caprock sealing in deep saline CO2 sequestration environments: a review study. J. Supercrit. Fluids 161, 104819.

JI, X., ZHU, C., 2013. Predicting possible effects of H2S impurity on CO2 transportation and geological storage. Environ. Sci. Technol. 47, 55–62.

JING, J., YANG, Y., CHENG, J., JING, X., DING, Z., 2024. Effects of injection temperature and pressure on CO2 storage capacity and safety in a sloping formation. Energy Fuels 38, 11891–11908.

JONAS, L., JOHN, T., KING, H.E., GEISLER, T., PUTNIS, A., 2014. The role of grain boundaries and transient porosity in rocks as fluid pathways for reaction front propagation. Earth Planet. Sci. Lett. 386, 64–74.

KAMPMAN, N., BICKLE, M., WIGLEY, M., DUBACQ, B., 2014. Fluid flow and CO2–fluid–mineral interactions during CO2-storage in sedimentary basins. Chem. Geol. 369, 22–50.

KAMPMAN, N., BUSCH, A., BERTIER, P., SNIPPE, J., HANGX, S., PIPICH, V., DI, Z., ROTHER, G., HARRINGTON, J.F., EVANS, J.P., MASKELL, A., CHAPMAN, H.J., BICKLE, M.J., 2016. Observational evidence confirms modelling of the long-term integrity of CO2-reservoir caprocks. Nat. Commun. 7, 12268.

KERMANI, B.M., MORSHED, A., 2003. Carbon dioxide corrosion in oil and gas production: a compendium. Corrosion 59, 659–683.

KUMAR, S., FOROOZESH, J., EDLMANN, K., REZK, M.G., LIM, C.Y., 2020. A comprehensive review of value-added CO2 sequestration in subsurface saline aquifers. J. Nat. Gas Sci. Eng. 81, 103437.

LAM, C.M., KUANJI, J.J., 2023. Repurposing of hydrocarbon pipelines for CO2 injection in CCS project – can it be done?. In: SPE Annual Technical Conference and Exhibition D021S021R001.

LAVINA, B., DERA, P., DOWNS, R.T., YANG, W., SINOGEIKIN, S., MENG, Y., SHEN, G., SCHIFERL, D., 2010. Structure of siderite FeCO3 to 56 GPa and hysteresis of its spin-pairing transition. Phys. Rev. B 82, 064110.

MACENTE, A., FUSSEIS, F., BUTLER, I.B., TUDISCO, E., HALL, S.A., ANDÒ, E., 2018. 4D porosity evolution during pressure-solution of NaCl in the presence of phyllosilicates. Earth Planet. Sci. Lett. 502, 115–125.

MACENTE, A., VANORIO, T., MILLER, K.J., FUSSEIS, F., BUTLER, I.B., 2019. Dynamic evolution of permeability in response to chemo-mechanical compaction. J. Geophys. Res. 124, 11204–11217.

MICHAEL, K., GOLAB, A., SHULAKOVA, V., ENNIS-KING, J., ALLINSON, G., SHARMA, S., AIKEN, T., 2010. Geological storage of CO2 in saline aquifers—a review of the experience from existing storage operations. Int. J. Greenh. Gas Control 4, 659–667.

MORLAND, B.H., DUGSTAD, A., SVENNINGSEN, G., 2022. Experimental based CO2 transport specification ensuring material integrity. Int. J. Greenh. Gas Control 119, 103697.

NÉEL, G., MILLET, C., RODRIGUEZ, D., SIMON, L., LIMA, L., 2022. Material selection for anthropogenic CO2 injection, mechanical and corrosion behavior of steels under CO2 with impurities. SSRN Electron. J.

NORDSVEEN, M., NESIC, S., NYBORG, R., A, S., 2003. A mechanistic model for carbon dioxide corrosion of mild steel in the presence of protective iron carbonate films—part 1: theory and verification. Corrosion 59, 443–456.

OGINO, T., SUZUKI, T., SAWADA, K., 1987. The formation and transformation mechanism of calcium carbonate in water. Geochim. Cosmochim. Acta 51, 2757–2767.

OZOTTA, O., KOLAWOLE, O., LAMINE MALKI, M., ORE, T., GENTZIS, T., FOWLER, H., LIU, K., OSTADHASSAN, M., 2022. Nano- to macro-scale structural, mineralogical, and mechanical alterations in a shale reservoir induced by exposure to supercritical CO2. Appl. Energy 326, 120051.

PAOLINELLI, L.D., PÉREZ, T., SIMISON, S.N, 2008. The effect of pre-corrosion and steel microstructure on inhibitor performance in CO2 corrosion. Corros. Sci. 50, 2456–2464.

PEARCE, J.M., HOLLOWAY, S., WACKER, H., NELIS, M.K., ROCHELLE, C., BATEMAN, K., 1996. Natural occurrences as analogues for the geological disposal of carbon dioxide. Energy Convers. Manag. 37, 1123–1128.

PENG, S., MARONE, F., DULTZ, S., 2014. Resolution effect in X-ray microcomputed tomography imaging and small pore's contribution to permeability for a Berea sandstone. J. Hydrol. 510, 403–411.

PESSU, F., BARKER, R., NEVILLE, A., 2015a. The influence of pH on localized corrosion behavior of X65 (UNS K03014) carbon steel in CO2-saturated brines. CORROSION. NACE International, Houston, Texas, Dallas, TX.

PESSU, F., BARKER, R., NEVILLE, A., 2015b. The influence of pH on localized corrosion behavior of X65 carbon steel in CO2-saturated brines. Corrosion 71, 1452–1466.

PESSU, F., BARKER, R., NEVILLE, A., 2020. CO2 Corrosion of carbon steel: the synergy of chloride ion concentration and temperature on metal penetration. Corrosion 76.

PESSU, F.O., SALEEM, E., ESPEJO, C., NEVILLE, A., 2022. Understanding the local pitting corrosion characteristics of carbon steel in CO2 corrosion environment using artificially machined pits. Results Eng. 16, 100700.

PETER, A., YANG, D., ESHIET, K.I.-I.I., SHENG, Y., 2022. A review of the studies on CO2–brine–rock interaction in geological storage process. Geosciences 12, 168.

M. A. RAZAK, A., A, A., SAAID, M., MD. YUSOF, I., HUSEIN, N., ZAIDIN, M.F., MOHAMAD SABIL, K., 2023. Physical and chemical effect of impurities in carbon capture, utilisation and storage J. Pet. Explor. Prod. Technol. 13, 1235–1246.

RENDEL, P.M., WOLFF-BOENISCH, D., GAVRIELI, I., GANOR, J., 2018. A novel experimental system for the exploration of CO2-water-rock interactions under conditions relevant to CO2 geological storage. Chem. Eng. J. 334, 1206–1213.

SHIRAKI, R., DUNN, T.L., 2000. Experimental study on water–rock interactions during CO2 flooding in the Tensleep Formation, Wyoming, USA. Appl. Geochem. 15, 265–279.

SONKE, J., BOS, W.M., PATERSON, S.J., 2022. Materials challenges with CO2 transport and injection for carbon capture and storage. Int. J. Greenh. Gas Control 114, 103601.
SUN, C., WANG, Y., SUN, J., LIN, X., LI, X., LIU, H., CHENG, X., 2016. Effect of impurity on the corrosion behavior of X65 steel in water-saturated supercritical CO2 system. J. Supercrit. Fluids 116, 70–82.
SUN, H., WANG, H., ZENG, Y., LIU, J., 2023. Corrosion challenges in supercritical CO2 transportation, storage, and utilization—a review. Renew. Sustain. Energy Rev. 179, 113292.
SUN, H., XU, Z., ZHANG, D., PENG, L., LAI, X., 2024. Corrosion behavior of passivation layer Cr2O3 of uncoated stainless steel under the anodic and cathodic conditions: a first-principles study. Chem. Eng. J. 493, 152658.
TANG, Y., HU, S., HE, Y., WANG, Y., WAN, X., CUI, S., LONG, K., 2021. Experiment on CO2-brine-rock interaction during CO2 injection and storage in gas reservoirs with aquifer. Chem. Eng. J. 413, 127567.
TUTOLO, B.M., LUHMANN, A.J., KONG, X.-Z., SAAR, M.O., SEYFRIED, W.E., 2015. CO2 sequestration in feldspar-rich sandstone: coupled evolution of fluid chemistry, mineral reaction rates, and hydrogeochemical properties. Geochim. Cosmochim. Acta 160, 132–154.
WANG, J., RYAN, D., ANTHONY, E.J., WILDGUST, N., AIKEN, T., 2011. Effects of impurities on CO2 transport, injection and storage. Energy Procedia 4, 3071–3078.
WANG, K., MA, L., TAYLOR, K.G., 2023. Microstructure changes as a response to CO2 storage in sedimentary rocks: recent developments and future challenges. Fuel 333, 126403.
WORDEN, R.H., 2024. Carbon dioxide capture and storage (CCS) in Saline aquifers versus depleted gas fields. Geosciences 14, 146.
YAN, T., XU, L.-C., ZENG, Z.-X., PAN, W.-G., 2024. Mechanism and anti-corrosion measures of carbon dioxide corrosion in CCUS: a review. iScience 27, 108594.
YARDLEY, B.W.D., 2009. The role of water in the evolution of the continental crust. J. Geol. Soc. 166, 585–600.
YONGZHI, Y.Z.Y.S.L.L.L.S.Y., 2012. An experimental study on water-rock interaction during water flooding in formations saturated with CO_2. Acta Pet. Sin. 33, 1032–1042.